

Unsteady flow and heat transfer through triply periodic minimal surfaces

Bruno Miguel Beja Guerra

Thesis to obtain the Master of Science Degree in

Mechanical Engineering

Supervisors: Prof. José Manuel da Silva Chaves Ribeiro Pereira
Prof. Miguel Abreu de Almeida Mendes

Examination Committee

Chairperson: Prof. Carlos Frederico Neves Bettencourt da Silva
Supervisor: Prof. Miguel Abreu de Almeida Mendes
Member of the Committee: Prof. Viriato Sérgio de Almeida Semião

September 2020

To my parents, for always loving and supporting me.

Acknowledgments

A special thanks to both my supervisors, Prof. Miguel Abreu de Almeida Mendes and Prof. José Chaves Ribeiro Pereira, for suggesting this subject to me, inserting me in the LASEF work-group, but mainly for all the effort invested in my work, and their valuable support since day one. To my colleagues at LASEF, thank you for your camaraderie and prompt support whenever needed.

While developing this work, but also in the five years that lead to it, I need to thank the group of friends that was always with me. The group of people that I will always keep in touch with, and lifetime friends who are always there in good and bad times.

Finally, I would like to thank my parents, two younger brothers, and Micaela for all the help during these years. Without them, this would not be possible. Thank you with all my heart.

Resumo

Novos avanços nos métodos de fabricação, como a impressão 3D, permitem a construção de novas espumas metálicas adequadas para o melhoramento do desempenho de permutadores de calor. As superfícies mínimas triplamente periódicas (SMTP) são ótimas candidatas à estrutura da espuma de um permutador de calor, porque separam o espaço em dois canais diferentes que se interconectam continuamente com uma área de superfície mínima, promovendo o uso mínimo de material com uma elevada transferência de calor. O presente trabalho recorre a simulações numéricas de escoamento incompressível 3D, através de estruturas porosas periódicas, constituídas por células cúbicas baseadas nas topologias Schwarz-D (SD) e Schoen-Gyroid (G) com múltiplas porosidades, entre 60 e 100%. Os resultados da simulação são obtidos cobrindo uma gama de números de Reynolds, desde escoamento laminar estacionário (regime de Darcy e Forchheimer moderado) até escoamento laminar não-estacionário (regime forte de Forchheimer). Múltiplas simulações com volumes elementares representativos (REVs) em diferentes posições, foram conduzidas para validar o cálculo de parâmetros macroscópicos para modelos de meios porosos utilizando apenas uma célula cúbica periódica unitária (apenas um REV). É obtida a localização da zona de transição para o regime laminar não-estacionário em função da porosidade. É proposta uma correlação para o número de Nusselt para a superfície Schoen-Gyroid (G) em escoamento laminar estacionário, para um intervalo de porosidades e números de Prandtl. Finalmente, a transferência de calor, a potência de bombagem e a eficiência das geometrias foram comparadas com o caso usual da placa plana, cobrindo o regime de escoamento laminar não-estacionário.

Palavras-chave: meios porosos, permutadores de calor, superfícies mínimas triplamente periódicas, mecânica dos fluidos computacional, escoamento laminar

Abstract

New advancements in manufacturing methods such as 3D printing, allow the construction and projection of novel metallic foams suitable for the improvement of heat exchangers performance that outperform those typically used. The Triply Periodic Minimal Surfaces (TPMS) are great candidates for the foam structure because they separate the space into two different channels that continually interconnect with a minimum surface area, promoting the minimum use of material with a high heat transfer. The present work deals with the numerical simulations of 3D incompressible flow through periodic porous structures, consisting of cubic cells based on the Schwarz-D (SD) and Schoen-Gyroid (G) topologies with multiple porosities between 60 and 100%. Simulation results are obtained covering a range of Reynolds numbers from laminar steady flow (Darcy and moderate Forchheimer regime) to laminar unsteady flow (strong Forchheimer regime). Multiple Representative Elementary Volume (REV) simulations in different positions were conducted to validate calculations of macroscopic parameters for porous media models carried out employing a unit periodic cubic cell (single REV). Transition region location to a laminar unsteady regime, as a function of porosity, is obtained. A correlation for the Nusselt number is proposed for the Schoen-Gyroid (G) surface in laminar-steady flow, for a range of porosities and Prandtl numbers. Finally, heat transfer, pumping power, and material efficiency were compared with the usual case of the parallel flat-plate covering the laminar unsteady flow.

Keywords: porous media, heat exchanger, triply periodic minimal surface, CFD, laminar flow

Contents

Acknowledgments	v
Resumo	vii
Abstract	ix
List of Tables	xiii
List of Figures	xv
Nomenclature	xvii
Acronyms	xix
1 Introduction	1
1.1 Motivation	1
1.2 Topic Overview	2
1.3 Objectives	3
1.4 Thesis Outline	3
2 Background	5
2.1 Modeling transport in porous media	5
2.1.1 Volume Averaging	6
2.1.2 Volume-Averaged Governing Equations	7
2.1.3 Analytical Flow Models	9
2.2 Fully Developed Internal Flow	11
2.3 Heat Exchangers	14
2.4 Numerical method	15
3 Implementation	17
3.1 Geometry Creation	17
3.2 Numerical Model	18
3.2.1 Pre-Processing	18
3.2.2 Solving	19
3.3 Verification and Validation	20
4 Results	23
4.1 Representative Elementary Volume	25

4.1.1	Location	25
4.1.2	Size	28
4.1.3	Procedure to compute low Péclet parameters	30
4.2	Steady to unsteady flow transition	32
4.2.1	Viscous and Inertial Permeability Coefficients	33
4.3	Correlations to Steady Laminar regime	37
4.4	Heat exchanger thermal performance	40
4.4.1	Pareto Efficiency	45
5	Conclusions	47
5.1	Achievements	47
5.2	Future Work	48
	Bibliography	49

List of Tables

3.1	Generated meshes for the grid independence study	21
4.1	Geometric properties of the analysed geometries (e.g. G80 corresponds to the Gyroid with a porosity of 80%).	25
4.2	Results obtained for the Nusselt average and estimate, deviation, error and computational reduction.	31
4.3	Permeability coefficients results.	35
4.4	Prandtl number and fluid properties.	37

List of Figures

1.1	Shell and tube heat exchanger (Left), Source: comsol.pt; Gyroid heat exchanger (Right)	2
2.1	REV (Left), Source: [21]; REV definition (Right), Source: [22]	6
2.2	Control volume for energy balance in a REV, source: [13].	12
2.3	Counter-flow heat exchanger (Left), Source: [13]; Condition for constant wall temperature (Right), Source: [13]	14
3.1	Surfaces created with <i>MathMod</i> ; Gyroid (left), Schwartz-D (right).	18
3.2	Hot, cold and solid domain (Left); Cold domain (Right).	21
3.3	Grid convergence for $Re_{p,D_h} = 100$ (Gyroid, $\phi = 100\%$).	21
3.4	Scheme of the 2D validation model.	22
3.5	Results of fully developed flow in parallel flat plates with constant wall temperature ($Pr = 2$).	22
4.1	Flat plate.	23
4.2	Schoen-Gyroid.	24
4.3	Schwartz-D.	24
4.4	Porosity ϕ , and Specific surface area a_{sf} , function of the wall thickness.	24
4.5	Movement of the REV along x-axis.	26
4.6	Different locations for the Gyroid and Schwartz-D surface REV.	27
4.7	Same cross-section for different Gyroid REV locations.	27
4.8	Nu_L for each different Gyroid surface REV ($Pr = 2.0$).	28
4.9	Nu_L for each different Schwartz-D surface REV ($Pr = 2.0$).	28
4.10	Cross-section temperature average (Gyroid, $\phi = 100\%$).	29
4.11	Correlation between velocity magnitude inlet and Nu_L (Gyroid, $\phi = 100$).	30
4.12	Scheme of the method proposed to compute Nu_L for a low Péclet number.	31
4.13	Three types of Residuals.	32
4.14	Transition location for the Gyroid surface depending on the porosity.	33
4.15	Dimensionless Darcy equation fitting.	34
4.16	Dimensionless Darcy-Forchheimer equation fitting.	35
4.17	Comparison between permeability data obtained for TPMSs (Gyroid and Schwartz-D) and literature correlation for porous materials. Data from Table 4.3.	35

4.18 Schoen-Gyroid. Variation of the ratio between the inertial and the total pressure drop identifying the steady, transition and unsteady regime ($\phi = 100\%$ and $\phi = 60\%$).	36
4.19 Schwartz-D. Variation of the ratio between the inertial and the total pressure drop identifying the steady, transition and unsteady regime ($\phi = 95\%$ and $\phi = 60\%$).	37
4.20 Comparison between correlations in literature and results obtained ($\phi = 60\%$, $Pr = 2$). . .	38
4.21 Results obtained for the Gyroid surface in the laminar steady regime.	38
4.22 Effect of porosity on coefficients a and b ($Pr = 2$).	39
4.23 Correlation and results obtained comparison.	40
4.24 Nu_{Dh} vs $Re_{p,Dh}$	41
4.25 Nu_L vs $Re_{Da,L}$	41
4.26 h vs $Re_{p,Dh}$	41
4.27 q_w/L^3 vs \dot{m}/L^2	42
4.28 ϵ vs $Re_{p,Dh}$	43
4.29 NTU vs $Re_{p,Dh}$	43
4.30 ϵ vs NTU	44
4.31 $1 - \epsilon$ vs L^3/q_w	44
4.32 $q_w/(\Delta P \dot{V})$ vs $Re_{p,Dh}$	45
4.33 L^3/q_w vs $(\Delta P \dot{V})/L^3$ ($Pr = 2$).	46
4.34 L^3/q_w vs $(\Delta P \dot{V})/L^3$ (Gyroid, $\phi = 100\%$).	46

Nomenclature

Greek symbols

α	Thermal diffusivity [m^2/s]
κ	Thermal conductivity coefficient [$\text{W}/\text{m K}$]
μ	Molecular viscosity coefficient [$\text{Pa}\cdot\text{s}$]
ϕ	Porosity
ψ	Extensive physical quantity
ρ	Density [kg/m^3]
τ	Tortuosity

Roman symbols

A_{Da}	Darcian inlet area [m^2]
L	Periodic length [m]
\dot{m}	Mass flow rate [kg/s]
Nu_L	Nusselt number based on the periodic length
$Pe_{Da,L}$	Péclet number based on the Darcian velocity and the periodic length
Pr	Prandtl number
$Re_{Da,L}$	Reynolds number based on the Darcian velocity and the periodic length
U	Velocity magnitude [m/s]
u, v, w	Velocity cartesian components [m/s]
V	Volume [m^3]

Subscripts

c	Cross-section; Cold
Da	Darcian

f	Fluid
h	Hot
i	Inlet
m	Mean value
o	Outlet
s	Solid
sf	Solid-fluid interface
w	Wall

Superscripts

$\langle \rangle$	Volume average
$*$	Dimensionless quantity

Acronyms

TPMS Triply Periodic Minimal Surface

REV Representative Elementary Volume

CFD Computational Fluid Dynamics

DNS Direct Numerical Simulation

FVM Finite Volume Method

SD Schwartz-D

G Schoen-Gyroid

Chapter 1

Introduction

Novel manufacturing methods allow the construction of geometries in the most varied ways. The present work is dedicated to a type of surfaces called Triply Periodic Minimal Surface (TPMS), and the objective is to numerically study the flow and heat transfer on these geometries, comparing the performance with other usual heat exchanger geometry, the parallel flat plate.

1.1 Motivation

Global energy consumption has been increasing every year, having a major impact on the demand for equipment with the highest energy efficiency [1]. This kind of equipment efficiency is essential today to fight the ever-growing energy consumption. Heat exchangers are one of the vital types of equipment used in various industries, including automotive and aerospace, chemical industry, oil and gas, power generation, refrigeration, among others [2]. Combined with new advancements in manufacturing methods such as additive manufacturing, building foams for the heat exchangers with an exact structure (e.g., periodic) is becoming a viable option for the industry [3]. It is now possible to produce new heat exchangers that outperform those typically used. The TPMS geometries are great candidates for the foam structure because they separate the space into two different channels that continually interconnect with a minimum surface area, promoting the minimum use of material with a high flow mix and heat transfer [4]. These TPMS geometries can be studied as a porous media [5]. Porous materials can be found in everyday life, all solids and quasi-solids are porous to some extent, which gives a higher significance for this work. As an example, porous structures for bone scaffolds are widely used in tissue engineering, providing being beneficial to cell growth rate, and a TPMS surface named gyroid that is studied in this work have demonstrated superior properties, and can be used for the structure of the bone scaffold [6]. As we can see, the study of the theory and characteristics intrinsic to the geometry itself as well as fluid flow and heat transfer through them assumes great importance.

The advances in computational processing power, that has been growing every year, allows for more precise numerical simulations leading to a better understanding of the physics behind the flow and heat transfer in such geometries [7]. For that reason, Computational Fluid Dynamics (CFD) analysis is the tool

of this work. The goal of this work and the focus throughout the document is to provide correlations and results for TPMS geometries that can be useful for the industry to manufacture novel heat exchangers.

1.2 Topic Overview

The study of porous media started in the XIX century with Darcy experimental approach to studying beds of sand. Nevertheless, the study of Darcy was limited by an upper limit of the validity of the flow velocity [8]. Attempting to solve this issue and determining a more extensive equation, Forchheimer proposed adding a quadratic term in the average velocity at high velocities as a mechanism to improve Darcy's expression [9]. Ergun [10] demonstrated the Forchheimer hypothesis experimentally and expanded the equation with the introduction of the hydraulic radius model, which defines a characteristic length of the porous media based on the void volume and surface area. Dybbs and Edwards [11] did a major experimental study in porous media defining a Reynolds number with a characteristic pore length and interstitial velocity and were able to distinguish between four different regimes in the Reynolds spectrum (Darcy, Inertial, Unsteady and Turbulent). The Local Volume-Averaging Method, which involves the integration over a Representative Elementary Volume (REV), of the conservation equations, was introduced by Whitaker [12]. Since these investigations, numerous applications dealing with heat and mass transfer across a porous media are being improved, such as combustion systems, evaporators, filtration systems, and heat exchangers. This work will deal with the latter.

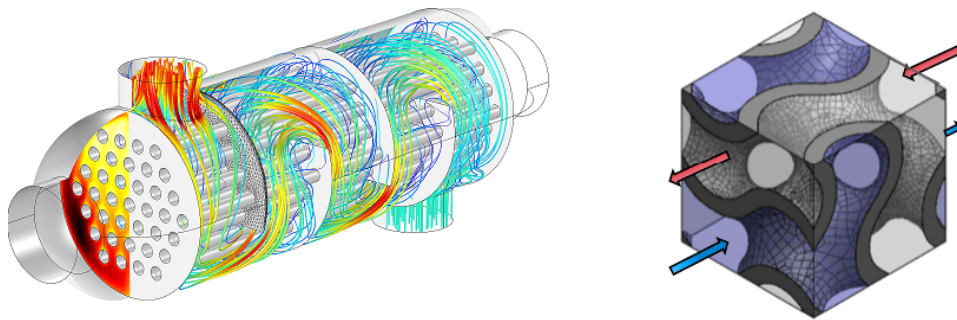


Figure 1.1: Shell and tube heat exchanger (Left), Source: comsol.pt; Gyroid heat exchanger (Right)

Heat exchangers are equipment that allow the transfer of heat between fluids at different temperatures. There are several classifications of heat exchangers, such as by type of construction or by flow arrangement. By the geometry of the structure, heat exchangers fall in several categories, including shell and tube, plates, and compact heat exchangers (Figure 1.1). About the classification of heat exchangers by flow arrangement, there are three categories: parallel-flow, counter-flow, and cross-flow [13]. Because there are many important applications, heat exchangers research and development, it always has put effort to achieve the best performance from this type of equipment based on two approaches. The first one with the use of new fluids like the nanofluids, i.e., fluids enriched with nanoparticles in order to increase the fluid thermal conductivity [14]. The second one is the focal point for this work, which includes the study for unique heat exchanger surfaces - e.g., Triply Periodic Minimal Surfaces - through heat transfer enhancement may be achieved [15].

A minimal surface is a surface that is locally area-minimizing; that is, a small section has the lowest possible area for a surface crossing the boundary of that section. The first description of minimal surfaces started with Euler and Meusnier in the XVIII century. The catenoid geometry discovered by the former and the helicoid by the latter [16]. Especially fascinating is that this kind of surface arises in natural structures such as soap films, bone tissue, and butterfly wings [6, 17]. In 1885, Schwartz and Neovius, described the first minimal surfaces that have a crystalline structure in the sense of repeating themselves in three dimensions, in other words being triply periodic [18]. The first Triply Periodic Minimal Surface include the Schwartz-D (SD), studied in this work. In 1970, the other TPMS studied in this work, the Schoen-Gyroid (G), is obtained by an algorithm derived by Schoen [19].

1.3 Objectives

The main objective of this work is to cover details of the pore-scale flow and heat transfer through TPMS to quantify physical parameters relevant for the design and performance evaluation of this type of surface applied to heat exchangers. The focus of the work can be divided into the following steps:

- Develop geometries from mathematical well defined TPMS with various wall thicknesses, to set an appropriate computational domain,
- Multiple simulations to study the influence of the Representative Elementary Volume (position and size) on the accuracy of the numerical estimations,
- Estimation of the permeability coefficients of TPMSs with the Darcy-Forchheimer law, to use for the prediction of transition region,
- Analyze the flow behavior of TPMSs in the unsteady regime,
- Develop a correlation that covers the inertial and Darcian region for various Prandtl and porosities,
- Heat exchanger design (heat transfer, pumping power, and material compactness), and identification of optimal minimal surfaces with focus on different flow regimes (covering laminar and unsteady flow regimes).

1.4 Thesis Outline

In this first chapter, the topics of the current work are presented, history and literature review of the subjects are summarized.

Chapter 2 provide the theoretical background regarding local volume averaging techniques, governing equations, and analytical flow models used on porous media. The theory of internal flow heat transfer and heat exchangers relevant parameters are also presented.

Chapter 3 explains the procedure used to make the TPMSs and from them obtain the solid geometries. Covers the numerical models implemented as well as the verification and validation process for the multiple simulations performed.

Chapter 4 presents the REV validity and procedure for the calculation of macroscopic parameters (Section 4.1), permeability coefficients results and unsteady flow analysis (Section 4.2), correlations obtained for the laminar-steady regime (Section 4.3), and results obtained of the heat transfer geometry parameters (Section 4.4).

The final chapter briefly describes the accomplished conclusions and suggestions for future work in this field of study.

Chapter 2

Background

This chapter presents the most relevant theoretical concepts necessary to understand this work better. In Section 2.1, the fundamentals and modeling of transport in porous media are introduced: volume averaging, governing equations, and analytical flow models. Heat transfer in internal flow are introduced in Section 2.2. The Section 2.3 presents the most important parameters for heat exchangers. Last Section 2.4 presents the approaches used in the literature to analyse porous media.

2.1 Modeling transport in porous media

A simple definition of a porous media consists of a solid matrix with void spaces that may be interconnect or not. The void volume may contain more than one phase, however, for simplicity, the focus will be towards single-phase flow systems. The macroscopic parameter that characterizes the media is the volumetric porosity defined by:

$$\phi = \frac{V_f}{V} \quad (2.1)$$

where $V = V_f + V_s$ is the total volume of the media, V_f is the void (fluid) volume and V_s is the solid volume.

The characteristic scale of the problem is the main aspect when considering the appropriate mathematical model. Continuity, momentum transport, and energy equations can be used if a representative number of pores is considered. To describe the system's microscopic phenomena at a macroscopic level (where quantities are measurable), a continuum approach may be applied. Kaviany [20] presented a relation from which the representative different lengths present in a porous medium are approximately governed by,

$$K^{\frac{1}{2}} \ll p < L \ll W, \quad (2.2)$$

$K^{\frac{1}{2}}$ is referred to as the Brinkman screening distance, which predicts the boundary layer thickness, i.e., gives the order of magnitude over which the velocity disturbance decays, p is the particle/pore

dimension, L is the size of a Representative Elementary Volume (REV) used to calculate macroscopic averaged values of extensive quantities. Finally, W is the system dimension, usually much larger than pore and REV size. The choice of the size of the REV is important to obtain meaningful values and relies on the condition that a change in volume in any given position does not affect the averaged quantity, and the REV size must be small enough to avoid fluctuations on the averaged quantity due to macroscopic heterogeneity's - Figure 2.1.

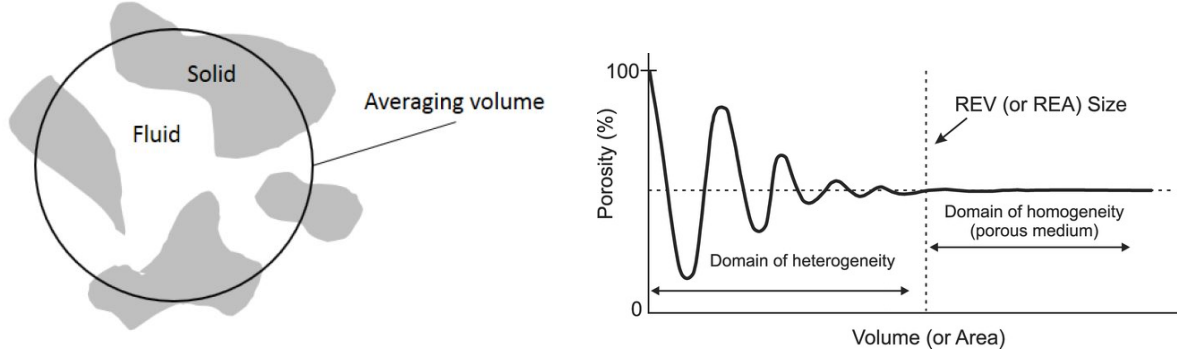


Figure 2.1: REV (Left), Source: [21]; REV definition (Right), Source: [22]

2.1.1 Volume Averaging

To arrive to the volume-average transport equations one must first define the volume-average theorem. Following the analysis presented by Bear and Bachmat [23], let ψ be a quantity associated to the fluid within the REV. There are two different averages to define. The volumetric phase average,

$$\langle \psi \rangle = \frac{1}{V} \int_{V_f} \psi dV, \quad (2.3)$$

and the volumetric intrinsic phase average,

$$\langle \psi \rangle^f = \frac{1}{V_f} \int_{V_f} \psi dV, \quad (2.4)$$

$\langle \psi \rangle^f$ is the value of $\langle \psi \rangle$ in the fluid phase and is, by definition, zero in the solid phase. The former is averaged over the entire domain and hence might be non-zero on the solid phase, while the latter is taken with respect to the fluid domain only. Both operations are integrated only over the fluid phase domain and may be related with porosity using the following equation:

$$\langle \psi \rangle = \phi \langle \psi \rangle^f, \quad (2.5)$$

Having defined the phase average over a REV of a quantity, the relation between the local value inside the volume and the average value is given by introducing the concept of fluctuation. The value a property has in a specific point can be described with the following equation:

$$\langle \psi \rangle = \langle \psi \rangle^f + \hat{\psi}, \quad (2.6)$$

where $\hat{\psi}$ is the deviation from the intrinsic phase average in the REV and $\langle \hat{\psi} \rangle = 0$ by definition. In section 4.1, we will see that for a low Péclet number, the definition is not always sustained.

For further analysis of the balance equations, the theorem for the volume average of a divergence is presented [24]:

$$\langle \nabla \cdot \psi \rangle = \nabla \cdot \langle \psi \rangle + \frac{1}{V} \int_{A_{sf}} \psi \cdot \vec{n} dA, \quad (2.7)$$

where \vec{n} is the unit normal to the area A_{sf} of the solid-fluid interface.

2.1.2 Volume-Averaged Governing Equations

The governing equations of fluid flow and heat transfer are the mathematical formulation of the conservation law of physics. The principle of mass conservation, Newton's second law of motion and the first law of thermodynamics [25].

Continuity Equation

The differential continuity equation takes the form,

$$\frac{\partial \rho}{\partial t} + \nabla \cdot (\rho \vec{U}) = 0, \quad (2.8)$$

where \vec{U} is the local velocity vector and ρ is the local fluid density. By volume-averaging the previous equation and no-slip boundary condition at the walls we get,

$$\frac{\partial \langle \rho \rangle}{\partial t} + \nabla \cdot \langle \rho \vec{U} \rangle = 0, \quad (2.9)$$

Momentum Equation

The change of momentum in a fluid element follows the Newton's second law,

$$\vec{F} = m \cdot \vec{a}, \quad (2.10)$$

This equation can be divided in spatial components and the different surface forces that can be applied in a fluid element, gravity force, pressure forces and viscous forces. In the case of a Newtonian fluid, the viscous stresses are proportional to the rates of deformation. These equation are known as Navier-Stokes equation, assuming constant fluid properties and incompressible flow, the equation is presented as:

$$\rho \frac{\partial \vec{U}}{\partial t} + \rho (\nabla \cdot \vec{U}) \cdot \vec{U} = -\nabla P + \mu \nabla^2 \cdot \vec{U} + \rho \vec{g}, \quad (2.11)$$

with P being the absolute pressure, g the body force and μ the dynamic viscosity. By volume averaging the equation (assuming porosity does not change in the averaging volume) is re-written as [26]:

$$\rho \frac{\partial \langle \vec{U} \rangle}{\partial t} + \rho \langle \nabla \cdot \vec{U} \vec{U} \rangle = -\langle \nabla P \rangle + \mu \langle \nabla^2 \cdot \vec{U} \rangle + \rho \vec{g}, \quad (2.12)$$

Using the decomposition 2.7 along with relations 2.5 and 2.6 it is possible to arrive after some algebra:

$$\rho \frac{\partial \langle \vec{U} \rangle}{\partial t} + \rho \langle \vec{U} \rangle^f \nabla \cdot \langle \vec{U} \rangle^f + \frac{\rho}{\phi} \nabla \cdot \langle \vec{U} \vec{U} \rangle = -\nabla \cdot (\langle P \rangle^f) + \mu \langle \nabla^2 \cdot \vec{U} \rangle^f + \rho \vec{g} + \frac{1}{V} \int_{A_{sf}} (-\hat{p} + \mu \nabla \vec{U}) \cdot \vec{n} dA, \quad (2.13)$$

Ruth and Ma [27] concluded that the third term on the left hand side of 2.13 may be relevant for macroscopic heterogenities or changes in porosity, and is associated with the hydrodynamic dispersion. In this work, the porosity is assumed to be constant and the term can be neglected.

Energy Equation

The first law of thermodynamics expresses that the rate of change of energy in a fluid element is equal to the sum of the net of heat exchanged and the net of work applied,

$$dE = dQ + dW, \quad (2.14)$$

The volume-averaged macroscopic energy equations are obtained for the solid and fluid phases from the work of Kuwahara et al. [28]. For the fluid and solid phase we have:

$$\phi \rho_f c_p \left[\frac{\partial \langle T \rangle^f}{\partial t} + \langle \vec{U} \rangle^f \cdot \nabla \langle T \rangle^f \right] = \nabla \cdot \left[\phi \kappa_f \nabla \langle T \rangle^f + \frac{1}{V} \int_{A_{sf}} \kappa_f T \cdot \vec{n} dA - \rho_f c_p \langle \hat{T} \hat{U} \rangle \right] + \frac{1}{V} \int_{A_{sf}} \kappa_f T \cdot \vec{n} dA, \quad (2.15)$$

$$(1 - \phi) \rho_s c \frac{\partial \langle T \rangle^s}{\partial t} = \nabla \cdot \left[(1 - \phi) \kappa_s \nabla \langle T \rangle^s - \frac{1}{V} \int_{A_{sf}} \kappa_s T \cdot \vec{n} dA \right] - \frac{1}{V} \int_{A_{sf}} \kappa_s T \cdot \vec{n} dA, \quad (2.16)$$

where the subscripts s and f denote the solid and fluid phase respectively, c is the solid specific heat, c_p is the fluid specific heat at constant pressure and k is the thermal conductivity. This two-equations model can be re-arranged, and be presented as follows:

$$\phi \rho_f c_p \left[\frac{\partial \langle T \rangle^f}{\partial t} + \langle \vec{U} \rangle^f \cdot \nabla \langle T \rangle^f \right] = \nabla \cdot (\bar{k}_{eff,f} \cdot \nabla \langle T \rangle^f) + h_{sf} a_{sf} (\langle T \rangle^s - \langle T \rangle^f), \quad (2.17)$$

$$(1 - \phi) \rho_s c \frac{\partial \langle T \rangle^s}{\partial t} = \nabla \cdot (\bar{k}_{eff,s} \cdot \nabla \langle T \rangle^s) + h_{sf} a_{sf} (\langle T \rangle^s - \langle T \rangle^f), \quad (2.18)$$

where $\bar{k}_{eff,f}$ and $\bar{k}_{eff,s}$ are the effective thermal conductivity tensors of the fluid and solid phase, re-

spectively, $a_{sf} = A_{sf}/V$ is the specific surface area, and h_{sf} is the interfacial convective heat transfer coefficient.

The interfacial convective heat transfer coefficient h_{sf} is calculated considering the volume averaged temperatures rather than the bulk mean temperatures of the fluid phase as it is usual for internal flows:

$$h_{sf} = \frac{\frac{1}{v} \int_{A_{sf}} \kappa_f T \cdot \vec{n} dA}{\langle T \rangle_s - \langle T \rangle_f}, \quad (2.19)$$

The temperature of the fluid, averaged in the space occupied by the fluid,

$$\langle T \rangle^f = \frac{1}{V_f} \int_{V_f} T dV, \quad (2.20)$$

2.1.3 Analytical Flow Models

For porous media, there is no consensus among authors on either the velocity or characteristic length for defining Reynolds number. Several authors have modified Re for incorporating structural features to better characterize the flow inside the medium. Due to a lack of consensus, it is difficult to choose a Re to compare and validate results.

In this work, four different definitions for the Re are used in different sections, combining two characteristic lengths with two velocities. The length of the REV L , and the characteristic pore lengths (hydraulic diameter D_h) are the two characteristic lengths. The Darcian velocity u_{Da} (velocity before the entry in the porous media), and the volume axial interstitial pore velocity average $\langle u \rangle$ (pore velocity), are the two velocities used to define the Re . Following the work of several authors [11, 29] the hydraulic diameter used in this work is defined by:

$$D_h = \frac{4\phi}{a_{sf}}, \quad (2.21)$$

The first Re used in the work, Section 4.1, is based on the Darcian velocity and length of the REV. Is used to compare results between different surfaces and geometries with the same imposed mass flow rate:

$$Re_{Da,L} = \frac{\rho u_{Da} L}{\mu}, \quad (2.22)$$

The Re based on the pore velocity and length of the REV depends only of the flow inside the pore because the length of the REV is the same for all geometries throughout the work. In Section 4.2 the sentence above is demonstrated with the results obtained for the transition points. Is also used in the correlation of Section 4.3:

$$Re_{p,L} = \frac{\rho \langle u \rangle L}{\mu}, \quad (2.23)$$

Another Re is based on the Darcian velocity and hydraulic diameter (equation 2.24). Is the Re less used in this work because has a similar behavior that the Re that is shown below (equation 2.25), that is

the main Re used in the literature of porous media.

$$Re_{Da,D_h} = \frac{\rho u_{Da} D_h}{\mu}, \quad (2.24)$$

According to Dybbs and Edwards [11] there are four flow regimes based on the pore and hydraulic diameter Reynolds number:

$$Re_{p,D_h} = \frac{\rho \langle u \rangle D_h}{\mu}, \quad (2.25)$$

- $Re_{p,D_h} < 1$, Darcy or creeping regime - Laminar steady,
- $1 - 10 < Re_{p,D_h} < 150$, moderate Forchheimer (or inertial) regime - Laminar steady,
- $150 < Re_{p,D_h} < 300$, strong Forchheimer regime - Laminar unsteady,
- $Re_{p,D_h} > 300$, unsteady chaotic - Turbulent.

For the laminar steady and laminar unsteady regime, the most studied regime and on the scope of this work, the pressure drop can be calculated using two equations: Darcy's law and the Darcy-Forchheimer law.

Darcy Flow Model

Henry Darcy in his experimental work with respect to groundwater flow has great importance, and his work led to the description of an experimental law [8]. The steady-state unidirectional flow experiments through a uniform bed indicated that the flow rate was proportional to the pressure gradient and can be expressed by Darcy's law:

$$\left(\frac{dp}{dx} \right) = \frac{1}{k_1} \mu u_{Da}, \quad (2.26)$$

with k_1 being the medium permeability given by a second-order tensor if the medium is anisotropic or by a constant if the medium is isotropic, which is the scope of this work. This value accounts for the ability of the fluid to pass through the medium. It is possible to derive Darcy's law from the Navier-Stokes equations provided that the inertial and time-dependent effects are neglected [30]. Darcy's law is valid in the creeping flow regime ($Re \ll 1$) and $Re = 1$ is an upper limit of validity for the Darcy law. Higher velocity flow regimes imply a need for a different relation for pressure drop and superficial velocity (Darcian velocity).

Forchheimer Flow Model

With the departure from the low velocities regime, the inertial forces cannot be neglected, and the form drag has to be considered as it is of the same order as the friction drag. Hazen [31] first proposed modifications to include the effects of temperature on viscous effects. However, it was Forchheimer in

1901 [9] that predicted that a non-linear term would have to be added. The non-linear term added results in a modification of Darcy's law:

$$\left(\frac{dp}{dx}\right) = \frac{1}{k_1}\mu u_{Da} + \frac{\rho}{k_2}u_{Da}^2, \quad (2.27)$$

where k_1 is Darcian permeability parameter defined previously, and k_2 are referred to as non-Darcian permeability parameter. The Darcy-Forchheimer law in the form of 2.27 is the general form of the expression, and several authors have been working on ways to complement it and proposing new equations [32–34]. With the Darcy-Forchheimer law, the complete laminar regime is covered until $Re = 300$. Although it is accepted that for steady-unsteady transition, Re_{tr} is around 150, can deviate from this value depending on the geometry, and the transition can be gradual and not a well-defined point [35]. This is studied later in work on Section 4.2.

Heat Transfer Foam Correlations

Kuwahara *et al.* [28], using the constant wall temperature boundary condition, which is used in this work, performed multiple simulations in staggered arrangements of square rods. The range of the parametric study is for porosities between $0.36 < \phi < 0.96$, Re numbers $3 \times 10^{-3} < Re_{Da,D_h} < 5 \times 10^3$ and Pr numbers $10 \times 10^{-2} < Pr < 10 \times 10^2$. Their heat transfer data were fitted by the correlation given by:

$$Nu_{D_h,K} = \left(1 + \frac{4(1-\phi)}{\phi}\right) + \frac{1}{2}(1-\phi)^{1/2}Re_{Da,D_h}^{0.6}Pr^{1.3}, \quad (2.28)$$

Gamrat *et al.* [36] reported simulations with constant wall temperature and found that their predictions were not in agreement with those of Kuwahara *et al.* [28]. The correlation obtained was the following:

$$Nu_{D_h,G} = 3.02(1-\phi)^{0.278}e^{2.54(1-\phi)} + ((1-\phi)1.093 + 0.357)Re_{Da,D_h}^{0.5}Pr^{0.3}, \quad (2.29)$$

2.2 Fully Developed Internal Flow

For an internal flow we must be concerned with the existence of entrance and fully developed regions. As a result of the development of the hydrodynamic and thermal boundary layers, four type of laminar flows occur: fully developed, hydrodynamically developing, thermally developing, and simultaneously developing. The former is the scope of this work, and the term fully developed flow refers to fluid flow in which both the velocity profile and temperature profile are fully developed (i.e., hydrodynamically and thermally developed flow) [37].

The hydrodynamic condition in the fully developed region is given by 2.30a. In heat transfer, the temperature is continuously changing with x , and it would seem that a fully developed condition could never be reached. A dimensionless form of the temperature is given to overcome that, 2.30b.

$$\left(\frac{\partial u}{\partial x}\right) = 0 \quad (2.30a)$$

$$\frac{\partial}{\partial x} \left[\frac{T_s(x) - T(x, y, z)}{T_s(x) - T_m(x)} \right] = 0 \quad (2.30b)$$

where $T_m(x)$ is the temperature mass flow average over the cross-section area (definition 4.4), T_s is the solid temperature, and $T(x, y, z)$ is the temperature in a point.

The pressure drop needed to sustain an internal flow is essential, as it is directly related to the pump or fan power requirements. It is convenient to work with the Moody friction factor, which is a dimensionless parameter defined from the Darcy–Weisbach equation [38]:

$$f = \frac{2 D_h \Delta P}{\rho u_m^2 L}, \quad (2.31)$$

where ΔP is the pressure drop across a distance L of porous media.

It is also important to introduce parameters that help understand the heat transfer phenomena when the internal flow is subjected to heat boundary conditions, *i.e.*, having a constant heat flux applied to or an imposed temperature on the wall of the porous media. The wall conductivity κ_s is high enough, compared to the fluid conductivity, to be considered infinite according to Shah and London [39], and hence the proper boundary condition to use in this work is constant wall temperature.

Energy balance applied to the porous media can be related to the difference in temperatures at the REV inlet and outlet to arrive to the heat transfer coefficient. Considering the flow inside the pore of Figure 2.2, moving at a constant flow rate, and convection heat transfer occurring at the inner surface. The differential control volume has a length dx , and expressing the rate of convection heat transfer to the differential element as $dq_{conv} = q_s'' P dx$, where P is the surface perimeter. The energy balance over an entire REV is given by:

$$q_{conv} = \dot{m} c_p (T_{m,o} - T_{m,i}) + q_{cond}, \quad (2.32)$$

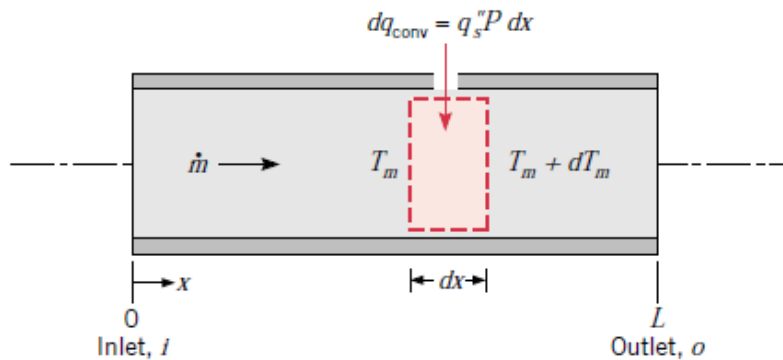


Figure 2.2: Control volume for energy balance in a REV, source: [13]

where q_{cond} can be neglected for a higher Péclet number (discussed later in Section 4.1), and the first term of the right hand side is the thermal energy advection between the inlet and outlet. In this work the

constant surface temperature is applied, and the expression for the average heat transfer coefficient is given by,

$$h_{sf} = \frac{q_{conv}}{A_{sf}(T_s - \langle T \rangle)}, \quad (2.33)$$

In heat transfer, the Prandtl number (Pr) quantifies the relation between momentum and heat diffusivity allowing a comparison between the two different boundary layers growth and it is defined as:

$$Pr = \frac{c_p \mu}{\kappa_f}, \quad (2.34)$$

In terms of evaluating the heat transfer, the Nusselt number is one of the most important parameters. It is defined as the ratio between heat transferred by convection to conduction across a fluid section.

$$Nu_{D_h} = \frac{h_{sf} D_h}{\kappa_f}, \quad (2.35)$$

The Nusselt number quantifies the amount of heat transfer, so a higher Nusselt number symbolizes an enhanced heat transfer by convection. There are multiple correlations to calculate Nu depending on the nature of the flow, although there is none applied to the case of minimal surfaces. Correlations for porous media foams are presented in the Section above 2.1.3. One objective of this work is to compute the TPMS Nusselt number and compare with the parallel flat plate.

Parallel Flat Plate

Laminar flow and heat transfer in parallel plate ducts are described in this section. The parallel plates have been analyzed in great detail by many authors [39–41]. The parallel plate geometry is a limiting geometry for the family of rectangular ducts and it forms an upper bound for fluid friction and heat transfer. Since these geometries are widely used in fluid flow and heat exchangers, the detailed analytical results for laminar flow and heat transfer for parallel plates are described below. The friction factor is given,

$$f = \frac{96}{Re_{D_h}}, \quad (2.36)$$

Nusselt number is constant, and given for practical calculations and comparison,

$$Nu_{D_h, T_m} = 7.54, \quad (2.37)$$

This value is calculated considering the temperature mass flow averaged T_m . In this work, the Nusselt is calculated with the temperature volume average $\langle T \rangle$, for a proper comparison with the results obtained for the TPMSs. For the parallel plate, the Nu value is slightly different from the above,

$$Nu_{D_h, \langle T \rangle} = 9.26, \quad (2.38)$$

2.3 Heat Exchangers

A heat exchanger is a device that is used for the transfer of thermal energy between two or more fluids, between a solid surface and a fluid, at differing temperatures and in thermal contact. In most heat exchangers, the fluids are separated by a heat transfer surface, and ideally, they do not mix. The special case of Figure 2.3 involves a counter-flow heat exchanger for which the hot fluid has a heat capacity rate much larger than that of the cold fluid, ($C_h \gg C_c$, $C = \dot{m}c_p$). The heat exchanger is studied as an internal flow with constant wall temperature.

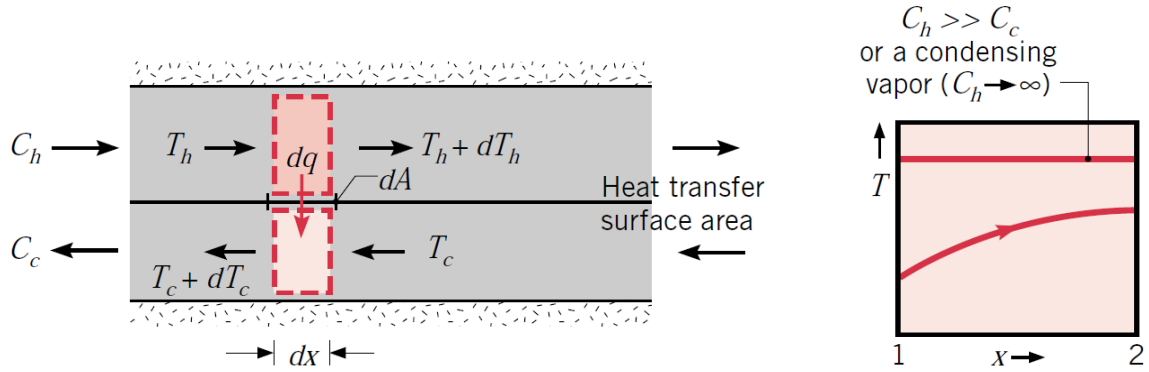


Figure 2.3: Counter-flow heat exchanger (Left), Source: [13]; Condition for constant wall temperature (Right), Source: [13]

Considering the fluid outlet temperatures or heat transfer rate as dependent variables, they are related to multiple independent parameters. Different methods for design and analysis of heat exchangers are available. However, this work deal with the $\epsilon - NTU$ method , and the most important parameters to characterize this method are presented.

The exchanger effectiveness ϵ is an efficiency factor. It is a ratio of the actual heat transfer rate from the hot fluid to the cold fluid in a given heat exchanger of any flow arrangement to the maximum possible heat transfer rate q_{max} thermodynamically permitted. The q_{max} is obtained in a counter-flow heat exchanger of infinite surface area.

$$\epsilon = \frac{q}{q_{max}}, \quad (2.39)$$

Equation 2.39 can be related with the fluid outlet and inlet temperature. Considering the case of Figure 2.3(b), the equation can be simplified to involve only one fluid:

$$\epsilon = \frac{T_{i,c} - T_{o,c}}{T_{i,c} - T_s}, \quad (2.40)$$

where $T_{i,c}$ and $T_{o,c}$ are the cold fluid inlet and outlet bulk temperature, respectively.

The number of transfer units (NTU) is a dimensionless parameter that is widely used for heat exchanger analysis [42] and is defined as:

$$NTU = \frac{h_{sf} A_{sf}}{\dot{m} c_p}, \quad (2.41)$$

Finally, the relation between ϵ and NTU for constant wall temperature is given by the expression:

$$\epsilon = 1 - \exp(-NTU), \quad (2.42)$$

The $\epsilon - NTU$ method approach for heat exchanger analysis provide no information concerning conditions within the exchanger. Although flow and temperature variations within a heat exchanger may be determined using commercial CFD (computational fluid dynamic) computer simulations.

2.4 Numerical method

Numerical simulations in porous foams might be divided into two branches, the ideal periodic simulations where one admits fully developed flow and simulates a REV with periodic conditions, and random foams [43]. Different numerical methods can be implemented to solve the flow field within the domain. Both Lattice-Boltzman [44], and Finite Volume Method (FVM) have been used, with the latter being discussed in further detail in the next chapter.

Krishnan [45] studied the laminar flow and heat transfer in a periodic open-cell structure solving all the spatial and temporal scales with Direct Numerical Simulation (DNS). The results compare reasonably well with the existing experimental models for higher porosities.

Diani et al. [46] simulated copper foams obtained from CT scan with the same porosity and different pore densities for the purpose of comparing the pressure drop and convective heat transfer with experimental results of the same foams and validate the CFD results for future work. They found that the pressure gradient varies with the velocity squared and higher pore densities equate to a bigger pressure drop since pores are smaller and the specific area is higher.

Della Torre et al. [47] simulated flow with real and ideal geometries covering laminar and turbulent regimes. It is noted that the pressure gradient as a function of Re_{p,D_h} is quadratic in both laminar and turbulent regimes, however, the viscous and inertial coefficients are distinct due to turbulence. To assess the influence of porosity and pore size, geometrical transformations were carried to modify the original foam. Permeability of the foam is found to increase exponentially with porosity while form drag decreases linearly.

Parthasarathy et al. [48] used CT scans to simulate pore-level flow examining pressure drop and tortuosity proposing a new Ergun type correlation based on the studied foams by adapting the viscous and inertial coefficients. Ruth and Ma [27] as already noticed that the inertial contribution is related to flow tortuosity.

Chapter 3

Implementation

This chapter is divided into three sections. It starts by describing the creation of the CAD model and how to obtain a TPMS, which is then imported into the CFD software. The following section describes the numerical models used in terms of meshing and physics. Finally, it presents the verification and validation process of the chosen models.

3.1 Geometry Creation

The first step of this work consists in creating the domain of the triply periodic minimal surfaces to perform the simulations.

Minimal surface structures are designed using *MathMod* software. The minimal surface representation of the Schwartz-D and Schoen-Gyroid, are approximated by the following nodal equations (several authors used the same approach [6, 49, 50]):

$$G : \cos(X)\sin(Y) + \cos(Y)\sin(Z) + \cos(Z)\sin(X) - n = 0, \quad (3.1)$$

$$SD : \cos(X)\cos(Y)\cos(z) - \sin(X)\sin(Y)\sin(Z) - n = 0, \quad (3.2)$$

where $X = 2\pi x/L$, $Y = 2\pi y/L$, and $Z = 2\pi z/L$. The parameter L decides the length of the cube in which the unit is located. The parameter n is introduced to create a solid surface wall with a homogeneous thickness, the surface are offset in the perpendicular direction to the surface normal vectors. When $n = 0$ the surface divides the space into two equal domains and approximates very well a truly minimal surface. A distinct advantage of using mathematical expressions to define these surfaces is that a desired number of parameters can be assigned to the model, so that a subsequent architecture optimization for porous materials study can be carried out with relative ease.

The minimal surfaces obtained with the software for a single unit cell are shown in Figure 3.1. The files are saved in *stl* format and can be processed in CAD software to obtain the desired geometry domain.

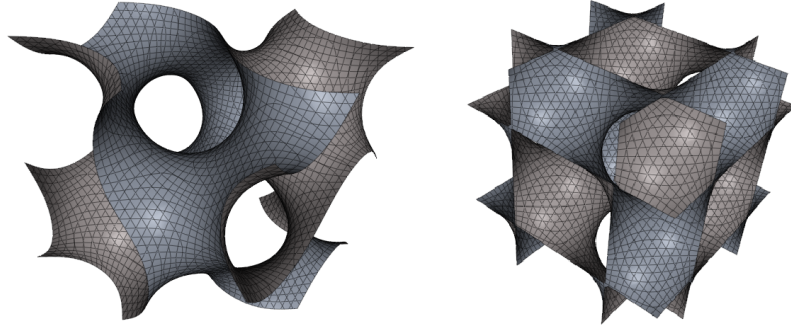


Figure 3.1: Surfaces created with *MathMod*; Gyroid (left), Schwartz-D (right).

The *stl* files of the surfaces are then imported into the CAD software SolidWorks to create the geometry of the fluid domain [51]. Finally, the fluid domain is transferred onto the CFD software to perform the simulation.

3.2 Numerical Model

Star-CCM+® [52] was the software used to create the domain of the porous media and run the numerical analysis. Comprises several packages with the capability to solve problems related to fluid flow, heat transfer as well as solid mechanics, therefore is a good choice for the current work and it will be used throughout the whole study for pre-processing, solving and post-processing.

3.2.1 Pre-Processing

First, the numerical domain was imported, and to preserve the flow a creation of multiple periodic interfaces in the fluid domain boundaries is necessary. The periodic interface between the inlet and outlet is then specified as a fully developed interface in which one period of the geometry is treated with the fully developed flow conditions, both hydrodynamic and thermal. Mass flow rate and bulk inflow temperature (293 K) are specified in the inlet. Another two periodic interfaces are defined in the boundaries normal to the y and z-axis with the symmetry condition. The solution that is obtained with a symmetry plane boundary is identical to the solution that would be obtained by mirroring the mesh about the symmetry plane. That together with the constant temperature condition defined in the wall boundary (328K) provide all the necessary extra equations required to close the system of equations.

The domain is discretized by the mesh construction and the software has the options to generate various types of meshes: Polyhedral, Tetrahedral, Trimmer, Extruder, and Prism Layer. A polyhedral cell mesh is used in this work since contains fewer cells for the same surface compared to tetrahedral and it is characterized for its stability and accuracy [53]. Trimmer is one that has minimal cell skewness and particularly useful for external aerodynamic flows given its ability to be refined in the wake region [54]. Extruder is typically used for inlet and outlet boundaries. It was also added to the mesh generation the prism layer. It generates orthogonal prismatic cells near wall surfaces, increasing the accuracy of

the solution in the near wall flow, making it a crucial tool to study heat transfer and boundary layer phenomena [55].

Regarding the physical model, the following assumptions were taken into account:

- Steady / Implicit unsteady, depending on the simulation,
- Three dimensional,
- Constant properties (ρ , μ , c_p and κ_f),
- Laminar,
- Segregated flow,
- Segregated fluid energy,

3.2.2 Solving

The governing differential equations need to be solved, and for that the equations are defined in terms of a general property ψ , allowing the definition of a transport equation of this quantity:

$$\frac{\partial \rho \psi}{\partial t} + \text{div}(\rho \psi \vec{U}) = \text{div}(\Gamma \nabla \psi) + S_\psi, \quad (3.3)$$

where the first term represents the rate of change of the quantity in the fluid element, the second term represents the net rate of the quantity flow, which means the convective flux. On the right side of the equation, the first term represents the diffusion rate and the final term represents a source term. Equation is then integrated over a control volume, on which the Gauss's divergence theorem is applied to the convective and diffusive terms resulting in:

$$\frac{\partial}{\partial t} \int_V \rho \psi dV + \oint_A \rho \psi \vec{U} dA = \oint_A \Gamma \nabla \psi dA + \int_V S_\psi dV, \quad (3.4)$$

The software solves discretised equations, using the Finite Volume Method (FVM) [56]. Algebraic relations are derived and that these, as approximations, will inherently conduce to error, the residual. In the discrete form the equation has the form of:

$$\frac{\partial}{\partial t} (\rho \psi V)_0 + \sum_f \rho \psi (\vec{U} \cdot \vec{a})_f = \sum_f (\Gamma \nabla \psi \cdot \vec{a})_f + (S_\psi V)_0, \quad (3.5)$$

The convective term is computed with a second-order upwind scheme. This scheme has high stability and second-order accuracy. The diffusive term is computed with the second-order central differences scheme. The transient term, which is zero during a steady-state solution, is approximated by a first-order temporal scheme that uses both the current time level and the previous one. The implicit solver is used.

The segregated flow model along with the SIMPLE algorithm (Semi-Implicit Method Pressure Linked Equations) is used to numerically solve the discretized equations in the form presented above. The steps of the algorithm procedure, in each iteration, implemented in the simulation, are summarized as follows:

- Boundary conditions input;
- Solving the discretised momentum equations to compute intermediate velocity field, u^* , v^* , w^* ;
- Solving of pressure correction equation to obtain, p' ;
- Update the pressure field as $p_{n+1} = p_n + \alpha p'$ with α being the pressure under-relaxation factor;
- Calculate u^* , v^* , w^* from the intermediate values with the velocity correction formulas;
- Calculate residual and test convergence;
- If convergence is not obtained, iterate again from point 2 with the pressure field equal to the one of the last iteration.

3.3 Verification and Validation

Wrong decisions based on CFD results can compromise projects, and have multiple consequences including wasting money, time and effort, and at the worst failure of components. To assess the level of confidence and quality of the numerical results, it is necessary for rigorous methods to measure the error and uncertainty. For that, the concepts of verification and validation have become methods that, nowadays, always go along with computational simulations.

The AIAA guide for verification and validation has had an important effect on the definition of these terms [57]. Roache [58] described validation as "solving the equations right", meaning that the errors are not due to lack of knowledge but instead by discretization errors, roundoff, or iterative convergence. Throughout all the simulations performed in this work, care was taken with the convergence of the simulation, watching the evolution of the residuals, setting a condition for them to drop two orders of magnitude per time step in the unsteady simulations. For the steady simulations, the convergence criteria were set for a minimum of 10^{-5} . Besides, variables of interest, such as the friction factor and Nusselt number were monitored to ensure convergence to average constant value - Figure 3.3. Validation, on the other hand, accesses whether the model used is an accurate representation of the real world. Was defined as "Solving the right equations" and the process quantifies the uncertainty. Its sources stem from inaccuracies due to an approximated geometry, material properties or boundary conditions as well as physical model uncertainty, as a result of inadequate representation of physical processes such as turbulence or simplifying hypothesis (e.g. steady flow, incompressible flow). It then requires highly accurate experimental measurements to validate a model.

To perform the verification, a grid independence study was executed on a Gyroid REV with a characteristic length of $L = 7mm$ and constant wall temperature is applied. For that reason, the simulations are only performed for the cold fluid domain 3.2. The geometry was designed to have a total maximum porosity of 100%. In order to evaluate grid convergence, a group of six meshes was evaluated. The mesh base sizes, which can be consulted on Table 3.1, start at 0.6mm and was further refined to an end base size of 0.1mm. All of the meshes were considered with polyhedral mesh and prism layer cells are added in the last meshes. Regarding the solid surface wall the no-slip condition was assumed.

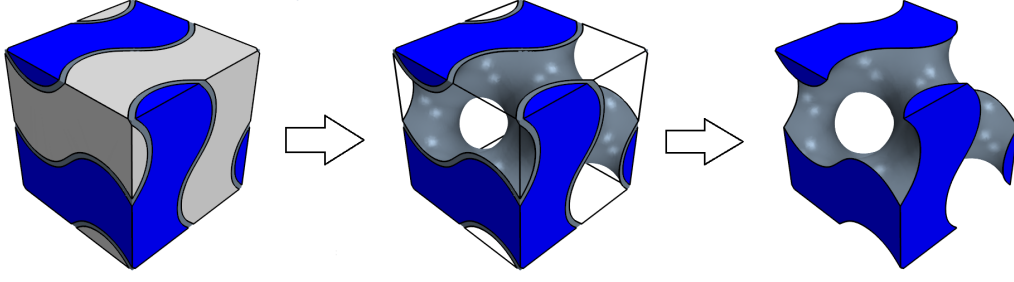


Figure 3.2: Hot, cold and solid domain (Left); Cold domain (Right).

Fluid properties for the verification were: $\rho = 1kg/m^3$, $\mu = 2 \times 10^{-5}Pa \cdot s$, $c_p = 1000J/kg \cdot K$ and $k_f = 0.01W/m \cdot K$. These values were chosen for having the resulting Prandtl number equal to 2. These properties were used throughout the work of this Thesis for almost every simulation, except in Section 4.3 as the influence of the Prandtl is studied.

Mesh No.	Base Size (mm)	Prism Layer Size (mm)	No. cells ($\times 10^5$)
1	0.60	0	1999
2	0.40	0	8658
3	0.20	0	34965
4	0.15	0	59162
5	0.15	0.1	76382
6	0.1	0.05	210411

Table 3.1: Generated meshes for the grid independence study

In order to evaluate whether convergence is attained the Darcy friction factor, and the Nusselt number based on the hydraulic diameter, were quantities calculated for each mesh. The results calculated for $Re_{p,D_h} = 100$ are shown on Figure 3.3.

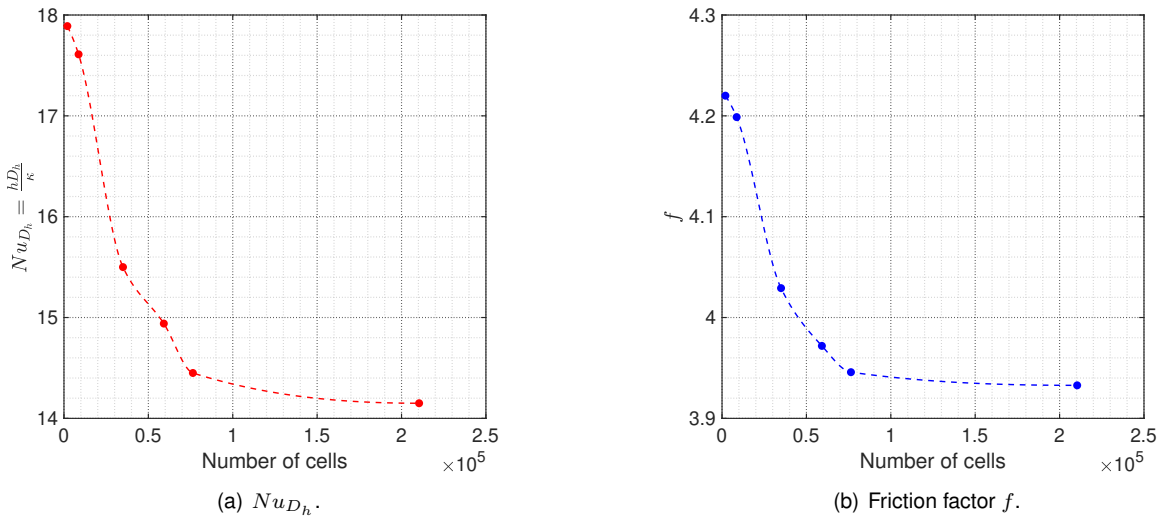


Figure 3.3: Grid convergence for $Re_{p,D_h} = 100$ (Gyroid, $\phi = 100\%$).

It can be concluded that there is no significant advantage in refining the mesh 5 further. The difference between mesh 5 and 6, regarding Nusselt number based on the hydraulic diameter, is 2.08% and regarding the Darcy friction factor of 0.51%. These differences are small compared to the computational effort difference from mesh 5 to 6, and for that reason, the mesh 5 is used throughout all work.

The validity of the model can be proven by comparing the present work results against literature values for similar geometries in terms of pressure drop and heat transfer. For that, 2D simulations of a parallel flat plate heat exchanger were performed. On the top and bottom walls, constant wall temperature is imposed. The flow was assumed to be fully developed in order to obtain the fully developed pressure drop along the channel and heat flux through the walls.

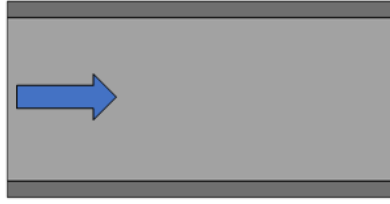


Figure 3.4: Scheme of the 2D validation model.

In Figure 3.5(a), it is shown the evolution of the friction factor with Re , and the results obtained are similar in relation to the theoretical curve described by $f = 96/Re$. For Nusselt number, the results are compared with the values referred in literature by Shah and London [39], and obtained considering the temperature mass flow averaged T_m . The results of the simulations compare very well with the theoretical values, particularly to $Pe_{p,D_h} > 30$, when the Nu_{D_h} tends towards a constant value of 7.54. As seen in Figure 3.5(b) to $Pe_{p,D_h} < 30$, the effects of axial conduction along the fluid become relevant, and the difference between the results in present work and the literature is a little higher, but the difference is not significant for this work.

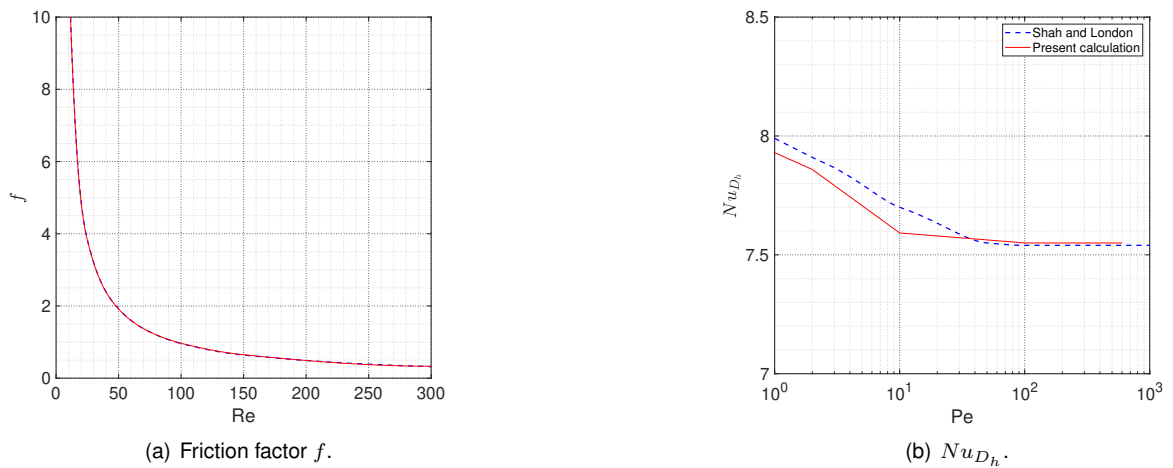


Figure 3.5: Results of fully developed flow in parallel flat plates with constant wall temperature ($Pr = 2$).

Since the agreement is satisfactory, the model assumptions hold, and the discretization errors are low enough for the intended analysis.

Chapter 4

Results

This chapter presents the achieved results and their discussion. First, analyzing the REV validity for the calculation of the macroscopic parameters. Permeability coefficients are obtained, followed by the study of the transition from steady to unsteady flow to get the critical point and zone of transition and their relation with the porosity. Thermal parameter correlations for the geometries are also obtained in this work for the steady-laminar regime. Last, the thermal performance in the unsteady regime is compared with the steady regime and the final analyses are to compare the energy trade-off between the heat exchanged (heat that cold fluid gets) and the pump power required to move the fluid across the geometry (pressure drop).

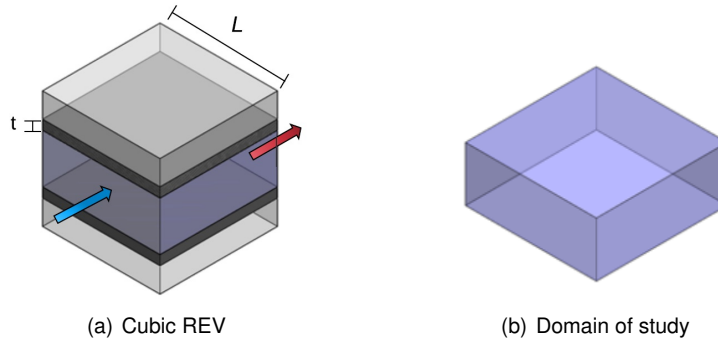


Figure 4.1: Flat plate.

To be compared with the TPMSs geometries analyzed in this work, a plate heat exchanger with a rectangular cross-section is taken because it is widely used in industrial processes [59]. The case test performed is an internal flow compacted with flat plates (top and bottom) with a cubic REV similar to the TPMSs analyzed in this work. In Figure 4.1(a), the cold flow direction is represented by the arrows, the top and bottom wall have both a boundary condition of constant wall temperature, and in Figure (b) the domain of the fluid simulated is represented.

The TPMSs chosen to be analyzed in this work are the Schoen-Gyroid (G) and Schwartz-D (SD). For the G surface, the effect of the porosity and the Prandtl number are analyzed in more detail, and for that reason, multiple porosities for the G surface are examined. In Figures 4.2, and 4.3, we can visualize that the simulation is only made for half the representative volume, i.e., for the cold fluid only.

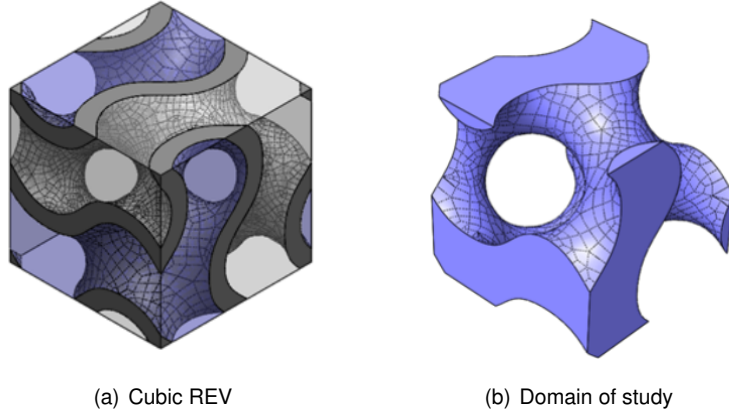


Figure 4.2: Schoen-Gyroid.

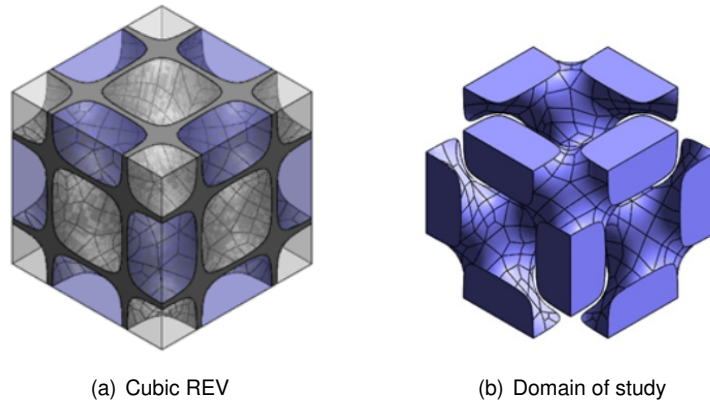


Figure 4.3: Schwartz-D.

In Figure 4.4, porosity ϕ , and specific surface area a_{sf} , as function of the wall thickness dimensionless with the length of the REV (t/L) is shown for the different surfaces. The parallel flat plate REV porosity and specific surface area have an exact function. For the SD and G surface, the results obtained for different geometries are fitted with a first-degree polynomial function for the porosity and second-degree for the specific surface area.

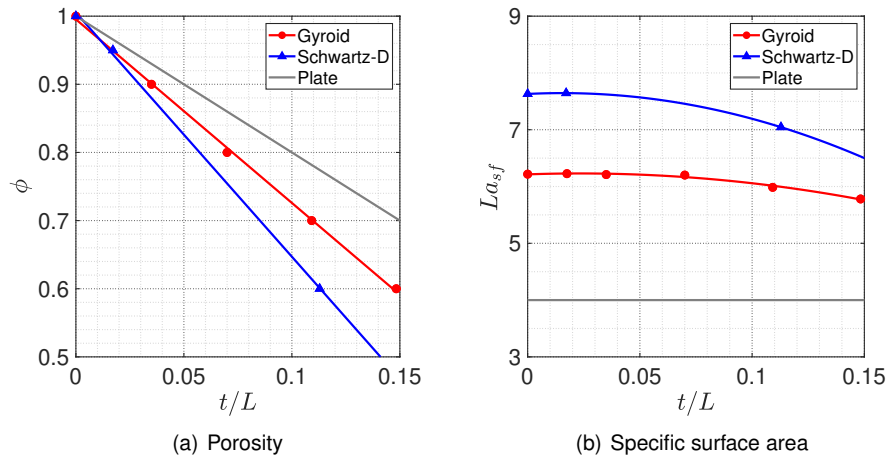


Figure 4.4: Porosity ϕ , and Specific surface area a_{sf} , function of the wall thickness.

Looking at Figure 4.4(a) we can see that for the same porosity, the wall thickness is different depending on the type of surfaces, being lower for Schwartz-D compared to Gyroid and the flat plate. Removing the value of the dimensionless thickness (t/L), for the same porosity, obtained for each surface and analyzing Figure 4.4(b), we can see that the SD surface has a bigger specific surface area and for the same porosity this difference is still greater compared to the specific surface area of G surface because the thickness is smaller (smaller value on the x axis). We can conclude that SD geometry has the largest contact area between the fluid and the wall for the same porosity or the same wall thickness.

Table 4.1 summarizes the most important properties of the analyzed geometries:

	<i>G100</i>	<i>G95</i>	<i>G90</i>	<i>G80</i>	<i>G70</i>	<i>G60</i>	<i>SD95</i>	<i>SD60</i>	<i>Plate</i>
ϕ	1.00	0.95	0.91	0.81	0.71	0.61	0.94	0.59	1.00
V_f [mm ³]	172	162	155	138	120	103	162	101	172
A_w [mm ²]	151.0	151.2	150.8	148.9	145.4	140.4	187.3	172.6	98.0
a_{sf} [m ⁻¹]	888.2	889.5	887.2	885.9	855.0	825.8	1092.1	1006.4	571.4
D_h [mm]	4.50	4.27	4.10	3.71	3.31	2.94	3.45	2.34	7.00
A_i [mm ²]	24.5	23.3	22.5	20.5	18.3	16.1	21.7	12.3	24.5
A_{avg} [mm ²]	24.5	23.1	21.8	19.7	16.9	14.5	23.0	14.4	24.5

Table 4.1: Geometric properties of the analysed geometries (e.g. G80 corresponds to the Gyroid with a porosity of 80%).

4.1 Representative Elementary Volume

For a proper study using a macroscopic approach, the choice of the correct averaging volume is essential, as mentioned in section 2.1. A relevant question is whether with the choice of a periodic unit cell for the REV, the results obtained for macroscopic parameters, such as Nu_L , are within an acceptable range of error. To evaluate this is necessary to analyze if the parameters are independent of the size and location adopted to the average volume.

In this section, the Péclet number definition used is with Darcian velocity u_{Da} (before the entry in the porous media) and with the length of the periodic structure L , because the value is the same, for different geometries, for a given mass flow rate. The definition is the following:

$$Pe_{Da,L} = Re_{Da,L} Pr = \frac{\dot{m}L}{\rho A_{Da} \alpha} \quad (4.1)$$

4.1.1 Location

Following the work of Teruel and Díaz [60], simulations for different locations of the averaging volume are carried out. They concluded that special care should be taken to compute parameters, mainly for low Péclet.

Different positions for the volume inlet were chosen along the x-axis as seen in Figure 4.5, giving

different elementary volume shapes and a different inlet surface (Figure 4.6). The distance covered along the x-axis corresponds to the length of the periodic structure to catch the multiple possible formats for the REV and the fluctuations in the macroscopic parameters. For each different inlet position, a simulation was performed.

It was found that the cross-sectional area of the TPMSs for the upper limit of $\phi = 100\%$ is constant, so the area average axial velocity u_m (equation 4.2) is constant for every given x. For a smaller porosity, the area of the cross-section along the REV is not constant. The G60 geometry has a difference of approximately 8% between the maximum and minimum value in relation to the average area A_{avg} , and u_m also changes in the same proportionality because the mass flow rate is constant and $\dot{m} = \rho u_m A_c$.

$$u_m = \frac{\int_{A_c} \rho u(y, z) dA_c}{\rho A_c} \quad (4.2)$$

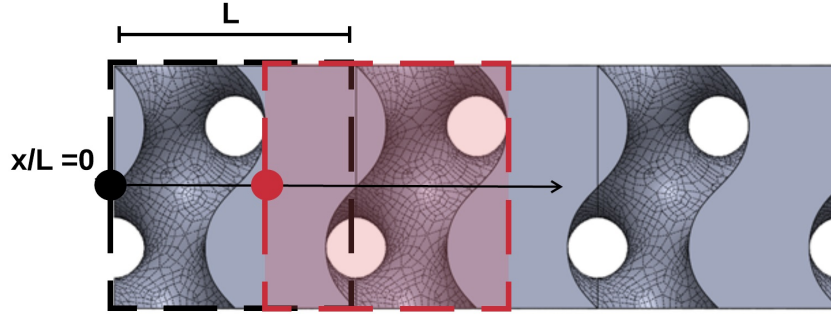


Figure 4.5: Movement of the REV along x-axis.

For fully developed hydrodynamic conditions, the change in the location of the periodic structure, doesn't change the dynamics of the flow. The flow pattern is independent of the chosen location for the entry of the periodic structure. Therefore for the equivalent cross-section, in a different REV (different simulation), for the same Pe , the velocity profile and magnitude is similar, as seen in the Figure 4.7.

The volume average of the interstitial velocity is equal for all periodic structures of the same geometry, both for the magnitude $\langle U \rangle$, and for axial direction. Due to the similarity of the flow, the pressure drop also does not depend on the position chosen for the REV. We can conclude that the location of the REV is independent for the hydrodynamic parameters like the pressure drop.

Figures 4.8 and 4.9 shows the Nu_L as a function of each REV inlet position (note that the abscissa corresponds to a non-dimensional length $x^* = x/L$). The dashed horizontal lines represent the calculated values of the $Nu_{L,avg}$ and $Nu_{L,est}$. Former is the mean of the fitting function, defined as the average value of the function over its domain (equation 4.3), and the latter will be discussed later in the Section 4.1.3.

$$Nu_{L,avg} = \frac{\int_0^L Nu_L(x^*) dx^*}{L} \quad (4.3)$$

Studying Figures 4.8(a) and 4.9(a), we can see that the variations in the parameters tend to decrease

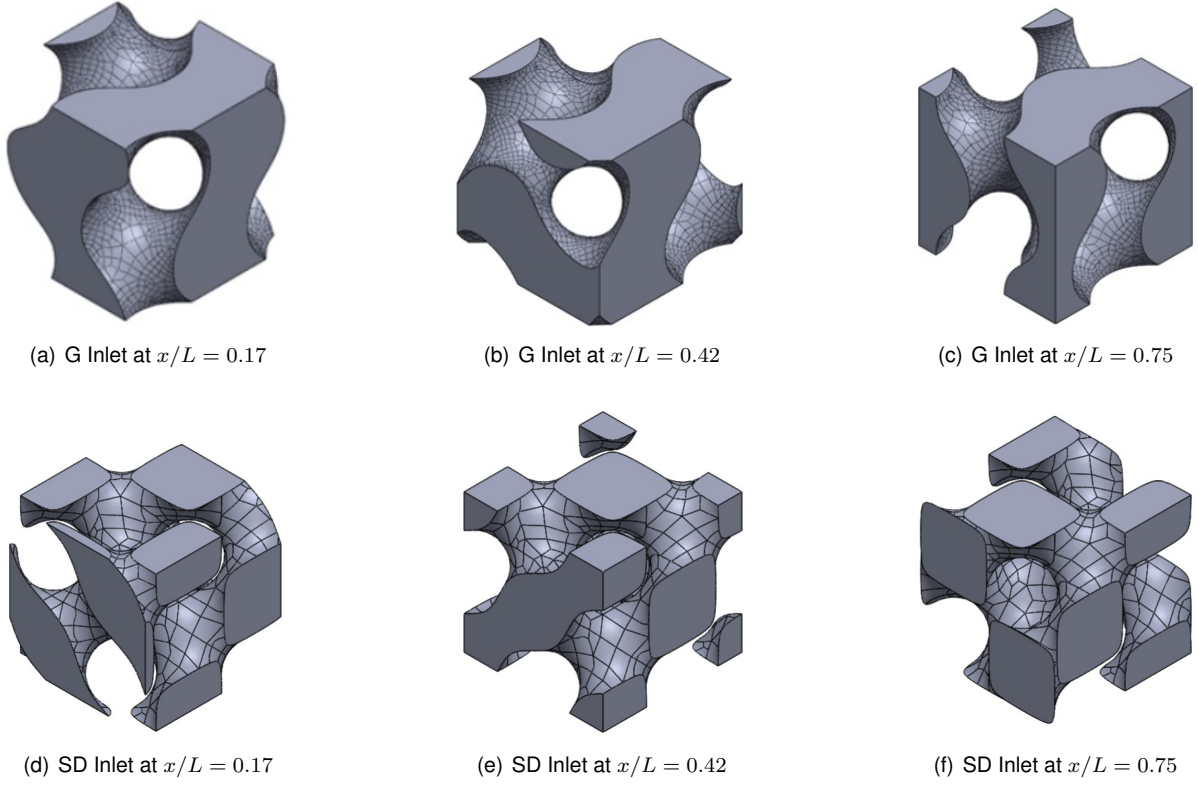


Figure 4.6: Different locations for the Gyroid and Schwartz-D surface REV.

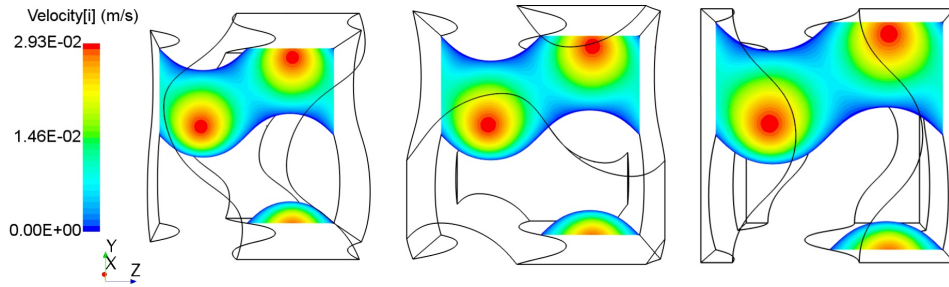


Figure 4.7: Same cross-section for different Gyroid REV locations.

with the increase of the Péclet, validating the results obtained by Teruel and Díaz [60] but for a different porous media geometry. For low Péclet numbers, the fluctuations in the parameters are higher, and for that reason, a single REV simulation can give results less approximate to the real value. In Section 4.1.3, a method for obtaining a more meaningful value is presented. Figure 4.8(b) and 4.9(b) compares the same surface with different porosities. For each one, the Péclet is the same, i.e., the forced mass flow rate is equal for each Figure. The former compares the G100 with the G60 geometry, and we can observe that for the G surface, the fluctuations are approximately equivalent for the same imposed mass flow rate, not depending on the porosity. For the latter, that compares the SD95 with the SD60 geometry, special care is needed computing the parameters for the SD surface because lower the porosity, higher the fluctuations are.

The variation in the thermal parameters can be explained due to the inlet boundary conduction. For different averaging volume inlet, the conduction in the inlet varies, and, for that reason, the heat transfer

in the wall boundaries also has to vary because the first law of thermodynamics cannot be infringed. This will be illustrated in the next section 4.1.3.

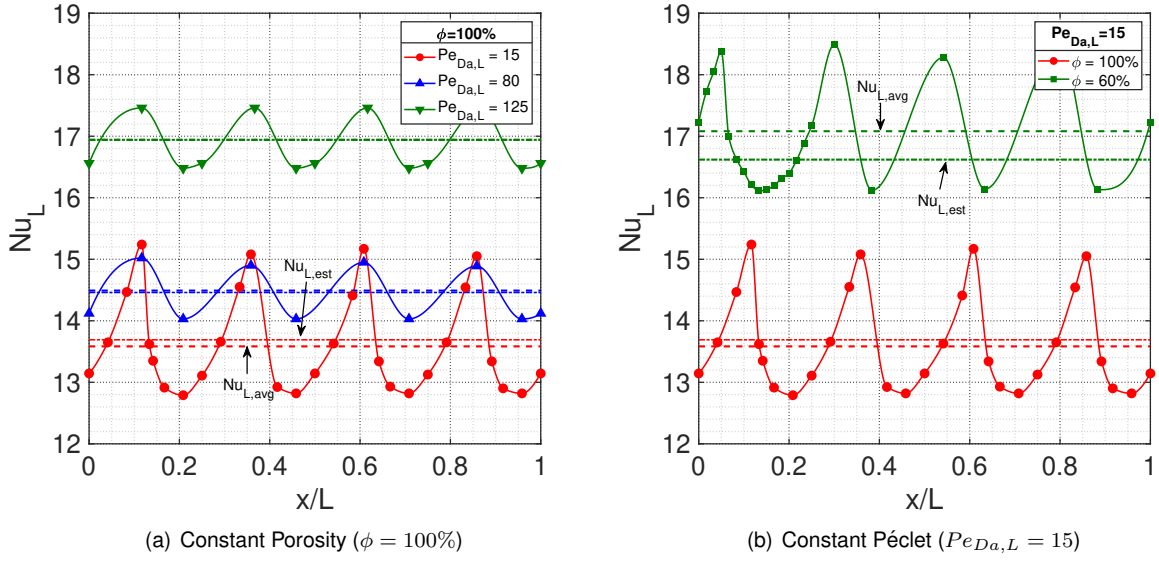


Figure 4.8: Nu_L for each different Gyroid surface REV ($Pr = 2.0$).

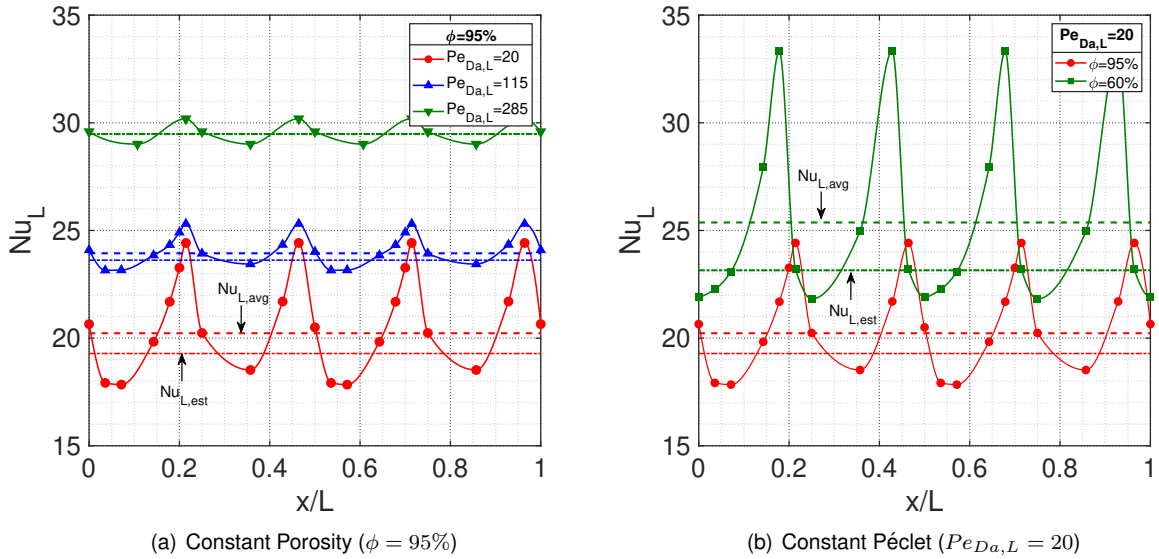


Figure 4.9: Nu_L for each different Schwartz-D surface REV ($Pr = 2.0$).

4.1.2 Size

The REV size must fulfill certain characteristics in order to represent the pore-scale flow. However, when dealing with periodic structures, the case is slightly different, given the periodicity of the structure. When dealing with these structures, one only has to guarantee that the simulation domain repeats itself and, in doing so, forms the complete structure. In this section, we will analyze whether the increase in the size of the REV is a solution to obtain better values of the parameters and fewer fluctuations, to have a

periodic structure independent of the location.

To study that, a simulation of a REV with two periodic structures (length of $2L$), and with the inlet at $x^* = 0$, is performed. In Figure 4.10 the x-axis represents a cross-section for the same simulation, and note that in the previous section represented the inlet for different REV simulations. The points of the average temperature T_m , for each cross-sectional area, are calculated by 4.4. The temperature difference for each section $\theta = T_w - T_m$, divided by the maximum possible temperature difference $\theta_i = T_w - T_i$, is a dimensionless form of the temperature average and may be defined as 4.5 [13].

$$T_m = \frac{\int_{A_c} \rho u c_p T dA_c}{\dot{m} c_p} \quad (4.4)$$

$$\theta^* = \frac{T_w - T_m}{T_w - T_i} \quad (4.5)$$

When analyzing Figure 4.10, we can see that increasing the size of the REV (two periodic structures in a row) is not one solution to find more accurate values of the parameters. The value obtained for Nu_L is approximately the same as for the simulation performed for the geometry with only one cell. The average temperature at the outlet of the first periodic cell can explain this result because it is already very close to the wall temperature. As a result, the heat transferred by the wall in the second periodic cell is almost zero and no longer has an impact on the convection coefficient h of the whole structure.

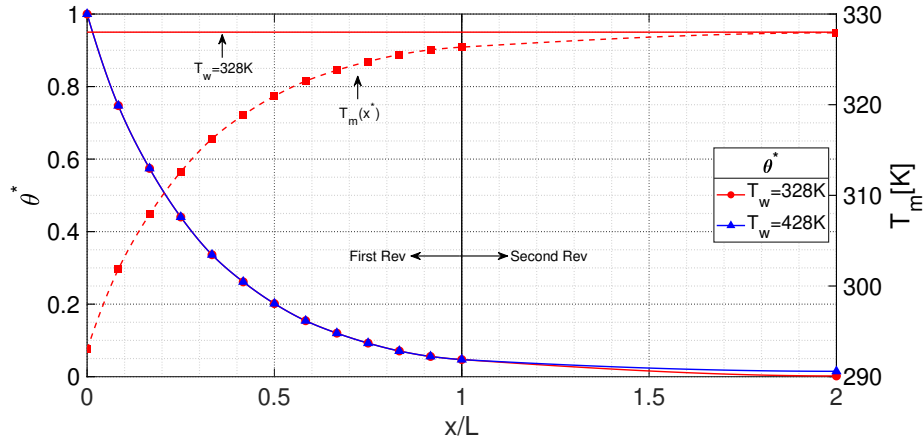


Figure 4.10: Cross-section temperature average (Gyroid, $\phi = 100\%$).

Another possibility could be to increase the temperature difference between the wall and the inlet flow. As we can see in Figure 4.10, the dimensionless temperature difference profiles are coincident, and for this reason, the Nusselt value is the same regardless of the temperature difference, as expected. With this result, we can conclude that the solution to obtain more approximate values for the parameters also does not involve increasing the temperature difference.

4.1.3 Procedure to compute low Péclet parameters

As mentioned in the previous Section 4.1.1, the variation of macroscopic parameters is only relevant for a low Péclet number. For this range of flows, the simulation of a single REV is not sufficient to compute and obtain the most accurate results for the thermal macroscopic parameters. In this section, a procedure will be presented with a less computational cost than doing the multiple simulations throughout the domain for different REV location.

In Figure 4.11 (results obtained for the G100 geometry), we can see that there is a relationship between the magnitude of the velocity at the REV inlet and the result obtained for Nu_L .

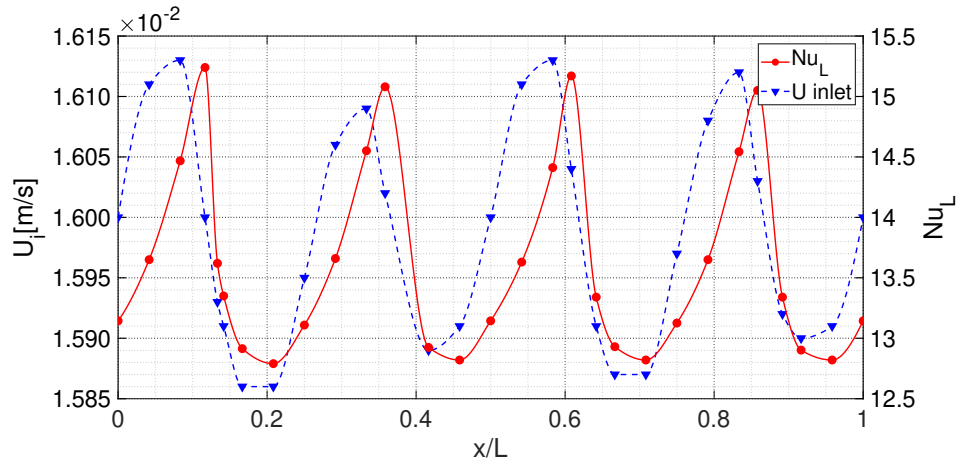


Figure 4.11: Correlation between velocity magnitude inlet and Nu_L (Gyroid, $\phi = 100\%$).

The method proposed (Figure 4.12) start with the creation of one periodic unit cell in any location of the porous media and performing a fluid flow simulation. This first simulation is needed to obtain the average velocity magnitude data along the REV cross-sections. Process the data to get the cross-section locations of the maximum (x_1) and minimum (x_2) average velocity magnitude. This locations are the same independently of the location of the periodic cell volume due to the flow similarity, as explained in the previous Section 4.1.1. After that, perform two more simulations, each one with the REV inlet location in the cross-sections obtained in the first simulation. Take the value of the Nu_L for each one and use the definition of equation 4.6 to calculate the $Nu_{L,est}$. The method described consists in making a total maximum of three simulations and has a much lower computational cost in contrast to the multiple simulations needed to get the $Nu_{L,avg}$.

$$Nu_{L,est} = \frac{Nu_L(U_{max}) + Nu_L(U_{min})}{2} \quad (4.6)$$

The following Table 4.2 summarizes the values of the maximum deviation D, between the value of the maximum Nusselt and the average Nusselt estimated with the two distinct definitions. More significant differences are found for low porosities and low Pe numbers. As we can see in the table, the error of the estimated Nusselt, in comparison with the $Nu_{L,avg}$ is not very pronounced. Hence, the procedure proposed in this section is reasonable for the computation of the parameters. We can also see that this difference tends to decrease with the increase of Péclet, as expected. Comparing the G with SD surface,

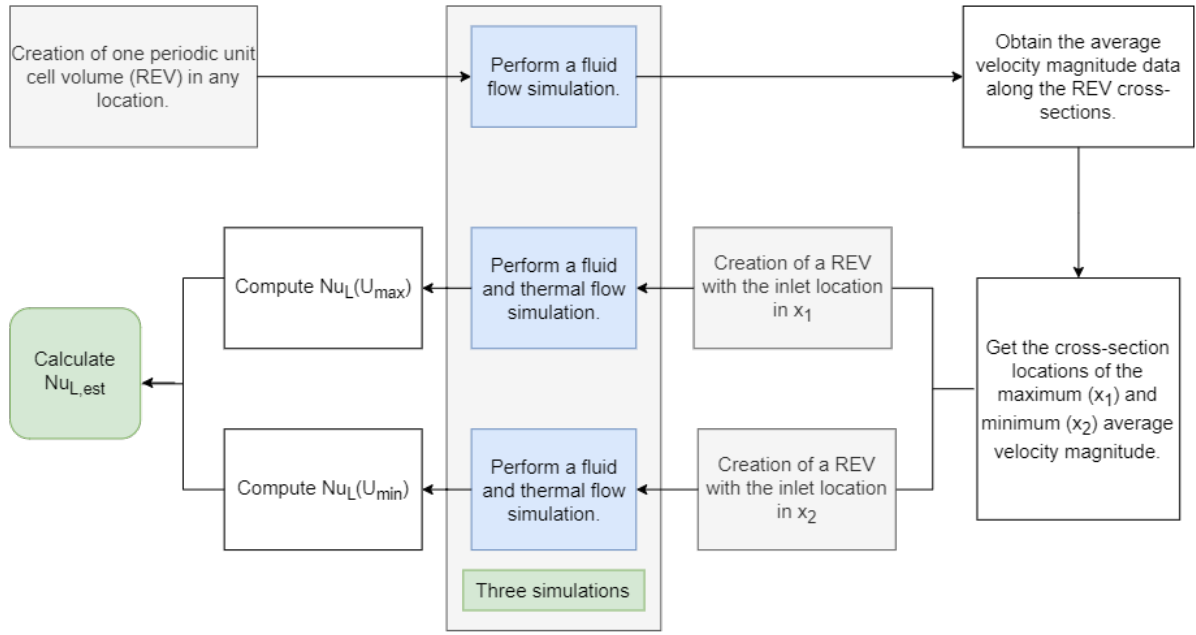


Figure 4.12: Scheme of the method proposed to compute Nu_L for a low Péclet number.

we can also see that for the same Péclet, the deviation is higher for the SD, that is, the fluctuations are higher for the SD surface.

To calculate $Nu_{L,avg}$ the simulations needed was always higher than 10, and the proposed method in this section only needs three simulations. Computational cost and time are greatly reduced with the method proposed in this section, as we can see in the last row of Table 4.2, and the values are calculated with $1 - 3/N$.

Geometry	G100			G60		SD95			SD60
$Pe_{Da,L}$	15	80	125	15	80	20	115	285	20
$Nu_{L,avg}$	13.6	14.5	16.9	17.1	20.1	20.2	23.9	29.5	25.4
$Nu_{L,est}$	13.7	14.5	16.9	16.6	19.9	19.3	23.6	29.5	23.2
$D_{avg} = \left \frac{Nu_{L,avg} - Nu_{L,max}}{Nu_{L,avg}} \right $	0.12	0.04	0.02	0.08	0.03	0.21	0.06	0.03	0.31
$D_{est} = \left \frac{Nu_{L,est} - Nu_{L,max}}{Nu_{L,est}} \right $	0.11	0.04	0.02	0.11	0.04	0.27	0.07	0.03	0.44
$Error_{est} = \left \frac{Nu_{L,est} - Nu_{L,avg}}{Nu_{L,avg}} \right (\%)$	0.8	≈ 0	≈ 0	2.7	0.9	4.7	1.33	≈ 0	8.8
$N = \text{Number of simulations}$	29	10	13	23	15	23	23	13	21
$\text{Computational reduction } (\%)$	90	70	77	87	80	87	87	77	86

Table 4.2: Results obtained for the Nusselt average and estimate, deviation, error and computational reduction.

4.2 Steady to unsteady flow transition

Thus far, in this Thesis, the transport and thermal properties of the porous media were obtained, assuming steady fluid flow with constant thermophysical properties. This section is divided into two parts. First, we will obtain the transition points for the G surface, followed by the calculation of the viscous and inertial permeability coefficients to obtain the Forchheimer number, Fo .

The transition from steady to unsteady flow does not have a well-defined point so that we will define in this work two distinct transition points [35]. The transition points are obtained in more detail for the G surface. The principal criterion to define these points is based on the residuals obtained in the simulations performed. Figure 4.13 represent the three different residuals behavior obtained to study the transition points. The first behavior (a) are achieved with the steady solver, the second (b) and third (c) with the unsteady solver.

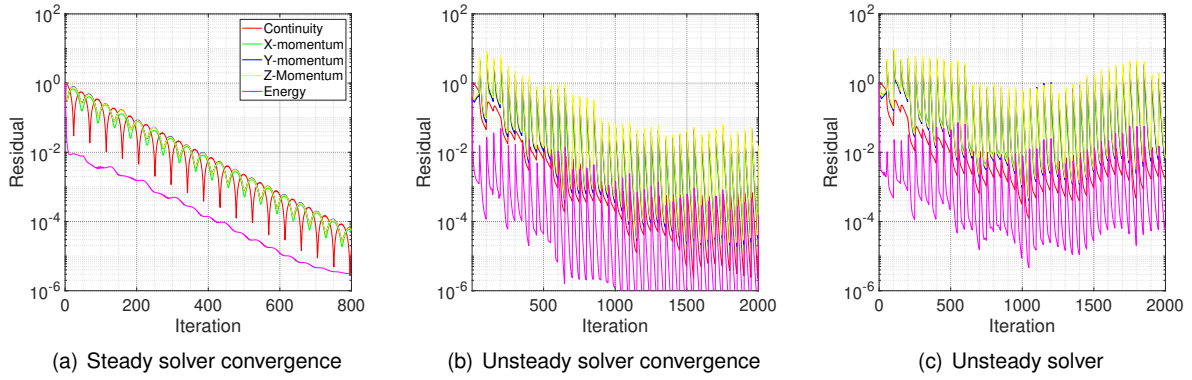


Figure 4.13: Three types of Residuals.

The first critical transition point is defined by running the steady solver, increasing the mass flow rate \dot{m} (Reynolds), until reaching a point where the residues diverge $Re_{tr,1}$. For the different porosities of the G surface, the values of the tortuosity, τ , and $Re_{tr,1}$ with four different definitions, are represented in Figure 4.14. The various definitions for Re are shown to demonstrate that special care is needed when comparing different porosities of a TPMS. As we can see in the Figure 4.14(a), the behavior of the Re value for transition point as a function of porosity depends on the definition used. What we can conclude is that when the porosity is higher, the critical point of transition occurs to higher flow velocity and has a broader range of the steady-laminar region. This effect can be explained due to the decrease in tortuosity for the same Reynolds. As seen in the previous Section 2.1.3, the transition point using the definition of $Re_{p,L}$ is approximately (due to errors in the numerical simulation) constant because depends only on the fluid flow inside the pore.

The second definition for the transition point $Re_{tr,2}$ is established by running the solution with the unsteady solver from the point where the steady solver simulation diverges, checking to what extent with the unsteady solver the simulation continues to converge as seen in Figure 4.13(c). The behavior of the τ and $Re_{tr,2}$ is very similar to the first transition point defined in this work, and the transition location is postponed to higher flow velocity (higher Reynolds) and higher tortuosity, as we can see in the Figure 4.14(b).

Tortuosity might be described by the ratio between the actual streamline and the straight line distance through the medium in the direction of the flow. To use this definition one would have to trace the particle trajectories and compare them with the straight line distance. An alternative was proposed which had into account the variables already calculated [61]. The equation is:

$$\tau = \frac{\langle U \rangle}{\langle u \rangle}, \quad (4.7)$$

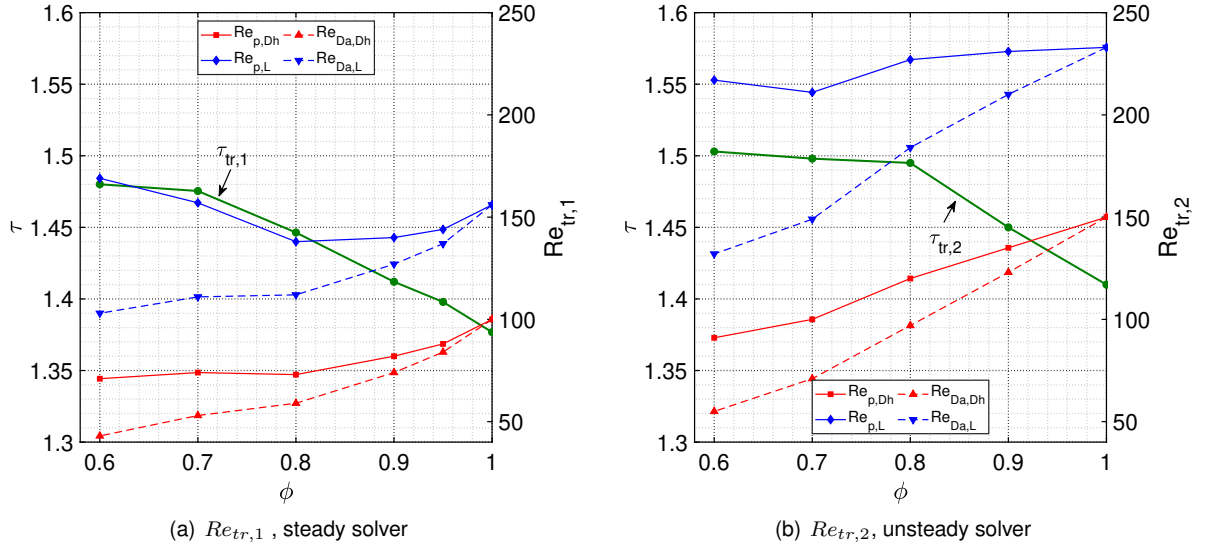


Figure 4.14: Transition location for the Gyroid surface depending on the porosity.

The next subsection is to verify and validate the results obtained for the transition points. Following the work of Eric et al. [62], we will use the definition of the number of Forchheimer 4.8, and the ratio between the inertial and the total pressure losses 4.9, to identify the transition zone and check if the methods used earlier in this section coincide with the results obtained by Eric et al.

$$Fo = \frac{\rho u_{Da} k_1}{\mu k_2}, \quad (4.8)$$

$$\frac{p_{inertial}}{p_{total}} = \frac{Fo}{1 + Fo}, \quad (4.9)$$

4.2.1 Viscous and Inertial Permeability Coefficients

When a high-velocity flow is present in the porous media, pressure drop follows the Darcy-Forchheimer equation, as seen in Section 2.1.3. For this equation to be meaningful and illustrative, accurate results of the Darcy permeability, k_1 , and the inertial coefficient, k_2 , must be obtained either by estimates given by correlations of geometric parameters or by data obtained from simulations. In this work, the latter is performed, and the simulation data will have to be fitted to the Darcy and Darcy-Forchheimer equation.

The first step was to simulate Darcy flow for $Re_{Dh} < 1$, and the pressure gradient was computed, such that the inertial contribution is negligible. To compute the Darcy permeability coefficient, k_1 , the

Darcy equation 2.26 is rearranged - dividing by $\rho u_{Da}^2 L$ - and a new dimensionalized pressure gradient is obtained given by equation 4.10. The equation is fitted with a linear polynomial, $1/Re_{Da,L}$ being represented in the x-axis, for all geometries studied in this work, as seen in Figure 4.15. Analyzing the results, we can see that the pressure drop for the creeping flow is higher for the Schwartz-D surface in comparison with the Gyroid surface and the parallel flat plate.

$$\left(\frac{dp}{dx}\right)^* = \frac{1}{k_1} \frac{1}{Re_{Da,L}}, \quad (4.10)$$

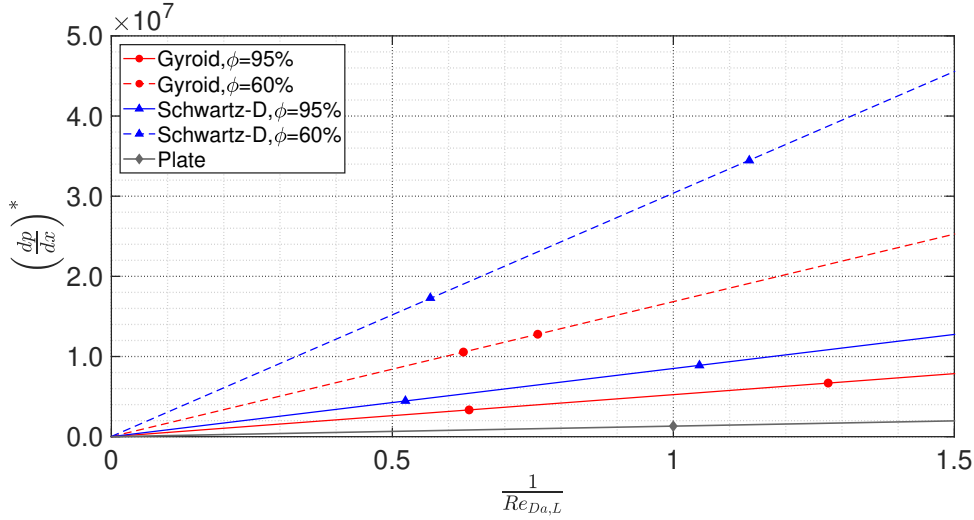


Figure 4.15: Dimensionless Darcy equation fitting.

To compute the inertial permeability coefficient, k_2 , the data obtained for pressure gradient in high-velocity flow $Re_{Dh} > 1$, is also fitted with a linear polynomial (Figure 4.16). Rearranging the Darcy-Forchheimer equation, the coefficient is calculated with 4.11. We can see that the k_2 coefficient is given by the intersection of the fitting with the y-axis. Comparing the pressure gradients of G and SD surfaces with the respective counterparts, the lower the porosity of the surfaces, the higher the pressure gradient will be. By Figure 4.16, we can also note that for a particular Re value, the pressure drop is higher in the G surface instead of the SD.

$$\left(\frac{dp}{dx}\right)^* = \frac{1}{k_1} \frac{1}{Re_{Da,L}} + \frac{1}{k_2} \frac{1}{L}, \quad (4.11)$$

The use of For to determine the validity of each permeability equation implies that both constants k_1 and k_2 must be available for analysis.

A substantial volume of permeability data based on Forchheimer's equation for highly porous media has become available in the literature and a correlation between both permeability parameters could link porous media of totally different structural features [29]. The equation is given by:

$$k_2 = \exp\left(-\frac{1.71588}{k_1^{0.08093}}\right), \quad (4.12)$$

In Figure 4.17, a comparison between permeability data obtained for TPMSs (Gyroid and Schwartz-D)

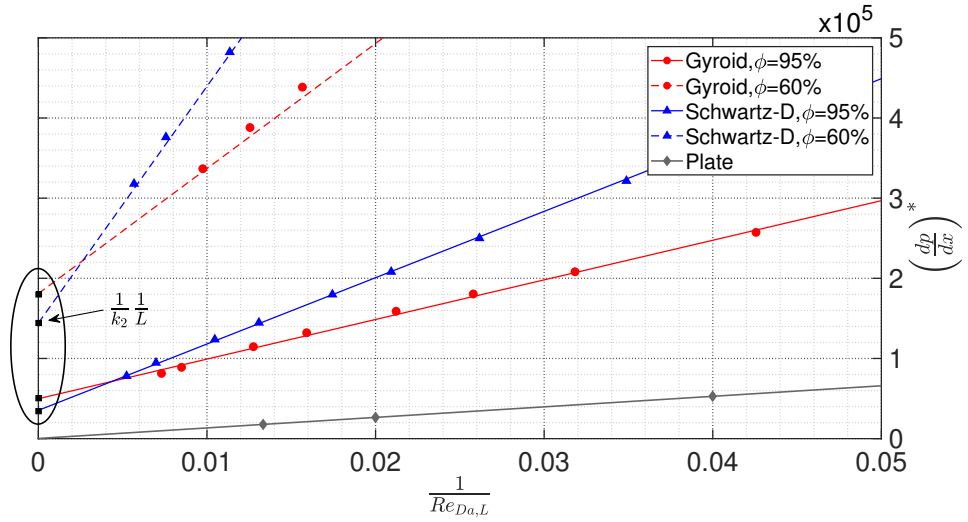


Figure 4.16: Dimensionless Darcy-Forchheimer equation fitting.

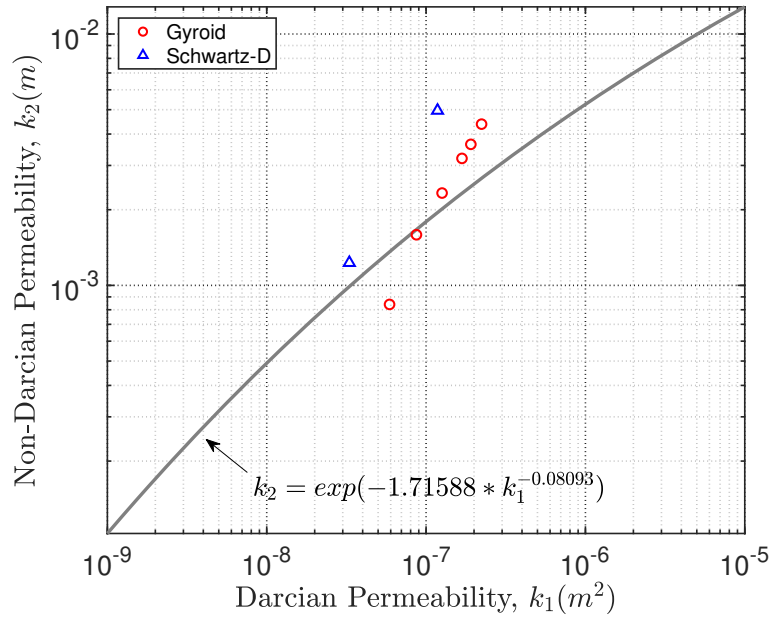


Figure 4.17: Comparison between permeability data obtained for TPMSs (Gyroid and Schwartz-D) and literature correlation for porous material. Data from Table 4.3

and literature correlation for porous materials is presented. We can see that the values obtained in this work for the permeability coefficients are validated with the literature correlation.

In the following Table 4.3, results of the permeability coefficients for all geometries studied in this work are presented:

	<i>G</i> 100	<i>G</i> 95	<i>G</i> 90	<i>G</i> 80	<i>G</i> 70	<i>G</i> 60	<i>SD</i> 95	<i>SD</i> 60	<i>Plate</i>
k_1 [$\times 10^{-7} m^2$]	2.23	1.91	1.68	1.26	0.87	0.59	1.18	0.33	7.61
k_2 [$\times 10^{-3} m$]	4.38	3.64	3.20	2.33	1.59	0.84	4.96	1.23	656.5

Table 4.3: Permeability coefficients results.

Eric et al. [62] concluded that the transition point for unsteady flow occurs when the inertial losses correspond to approximately 60% of the total losses ($Fo/(1+Fo) = 0.6$). In Figure 4.18 the data obtained for two different geometries of the Gyroid are represented - G100 and G60. All considered simulations are indicated on a curve that shows the variation in the ratio between the inertial and the total pressure drop as a function of the Forchheimer number. The green dots represent the results obtained with the steady solver, that is, the laminar-steady regime. The blue dots represent the points for simulations with the unsteady solver, but that converge to steady. We term this the transition zone. The red dots already represent points in the unsteady regime. As we can see, the transition zone is around the point where the inertial losses correspond to 60% of the total losses, thus validating the results obtained in the previous Section.

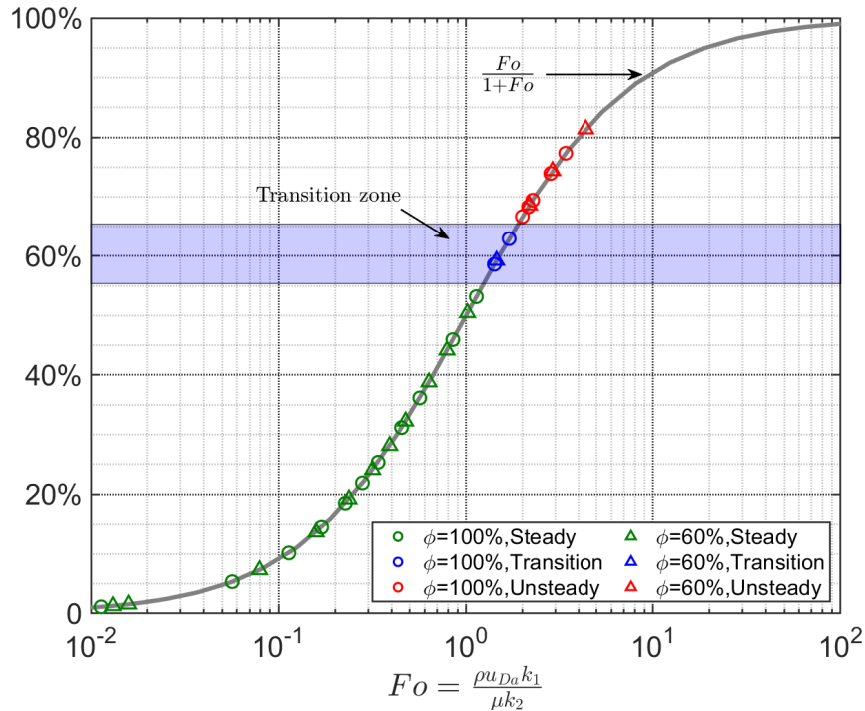


Figure 4.18: Schoen-Gyroid. Variation of the ratio between the inertial and the total pressure drop identifying the steady, transition and unsteady regime ($\phi = 100\%$ and $\phi = 60\%$).

In Figure 4.19 the data obtained for two different geometries of the Schwartz-D are represented - SD95 and SD60. The transition zone, like the G surface, is around the point where the inertial losses correspond to 60% of the total losses. For a higher porosity, the transition zone begins for a lower Fo . Due to this reason, the SD has a higher range of values in the transition zone in comparison with the G surface.

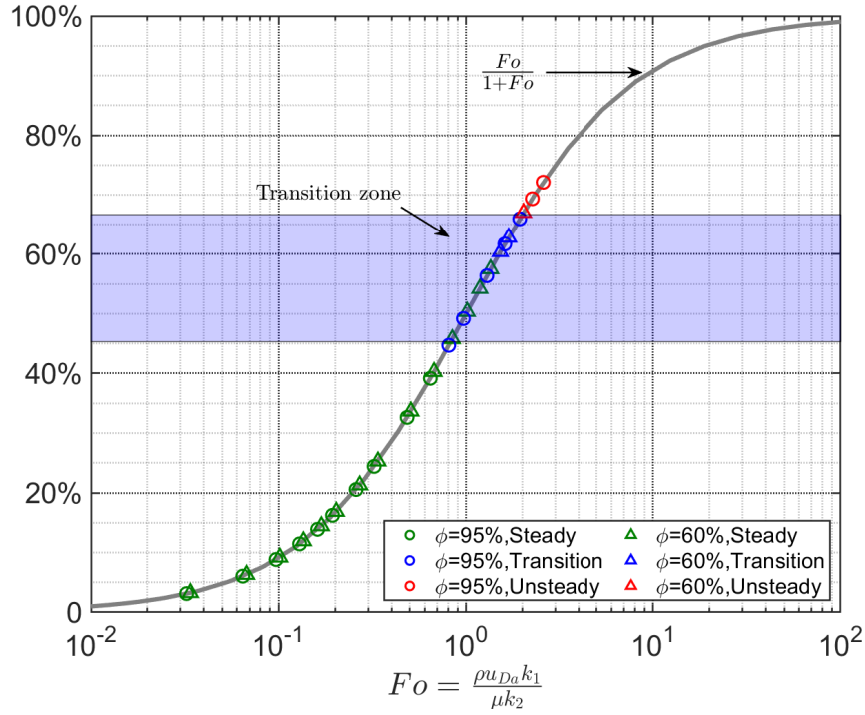


Figure 4.19: Schwartz-D. Variation of the ratio between the inertial and the total pressure drop identifying the steady, transition and unsteady regime ($\phi = 95\%$ and $\phi = 60\%$).

4.3 Correlations to Steady Laminar regime

In this section, a correlation for the Gyroid surface, for the laminar steady regime, is computed and compared with other correlations described in the literature for porous media reported in Section 2.1.3 by the equations 2.28 and 2.29. Simulations were performed for various Prandtl numbers, and among them the Pr of water and air. The properties are described in Table 4.4.

Prandtl	Density $\rho, (kg/m^3)$	Viscosity $\mu, (Pa \cdot s)$	Conductivity $\kappa, (W/m \cdot K)$	Specific heat $c_p, (J/kg \cdot K)$	Thermal diffusivity $\alpha, (m^2/s)$
7	1000.0	1e-3	0.597	4180	1.40e-7
2	1.0	2e-5	0.01	1000	1.00e-5
0.7	1.0	2e-5	0.0286	1000	2.86e-5

Table 4.4: Prandtl number and fluid properties.

Comparison between correlations in literature and results obtained for the G60 and SD60 geometry, both with a $Pr = 2$ are shown in Figure 4.20. Analysing the results obtained, we can conclude that for $Re > 20$ the behavior of the correlations are in line with the obtained results for the Nusselt, and the expression of Kuawahara et al. has a minor difference from the values obtained in this work. But, our study based multiple numerical simulations suggests that a separate correlation should be established for correlating the data obtained.

The correlations mentioned above are obtained with the number of Re_{p,D_h} as a variable. In Section

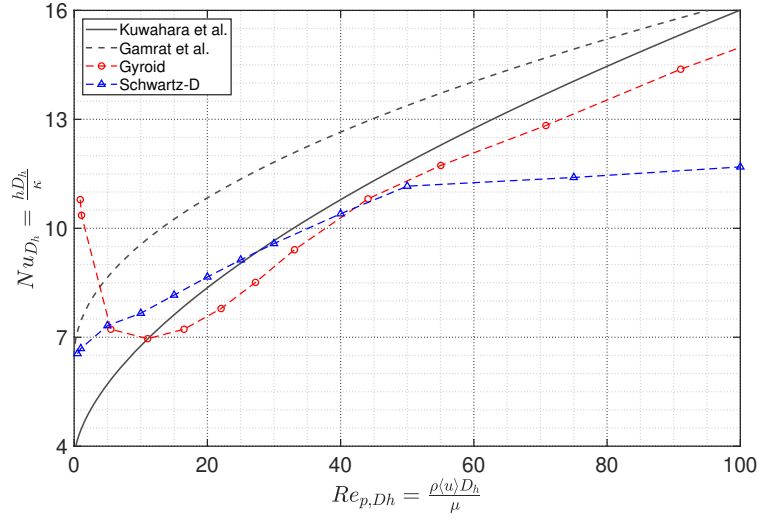


Figure 4.20: Comparison between correlations in literature and results obtained ($\phi = 60\%$, $Pr = 2$).

4.2 we saw that the transition point varies for different porosities with this definition of the number of Re . Using the characteristic length of the periodic cell L , and the interstitial velocity $\langle u \rangle$ to define the number of Re , the transition point is practically constant as we can analyze in Figure 4.14. Due to this factor, the correlation that is obtained for the Gyroid in this work takes the form of Equation 4.13. The scope of this section is obtain the coefficients (a , b , m , n) that best fit the results.

$$Nu_L = a + b Re_{p,L}^m Pr^n, \quad (4.13)$$

In Figure 4.21, the results obtained for various Gyroid surface porosities are shown. Before obtaining a expression for the coefficients a and b is necessary to work with this results and obtain the coefficients m and n . Processing and fitting the plots obtained, the achieved values is $m = 0.79$ and $n = 0.36$.

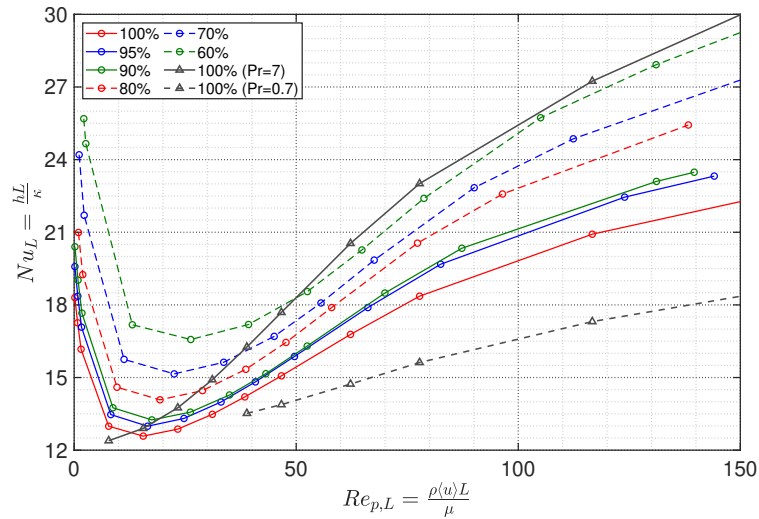


Figure 4.21: Results obtained for the Gyroid surface in the laminar steady regime.

$$Nu_L = a + bRe_{p,L}^{0.79}Pr^{0.36}, \quad (4.14)$$

The next step is to obtain the coefficients a and b . For that, a fitting is done with the form reached above 4.14, and a value is obtained for the coefficients. This procedure is done for every porosity with a constant Pr .

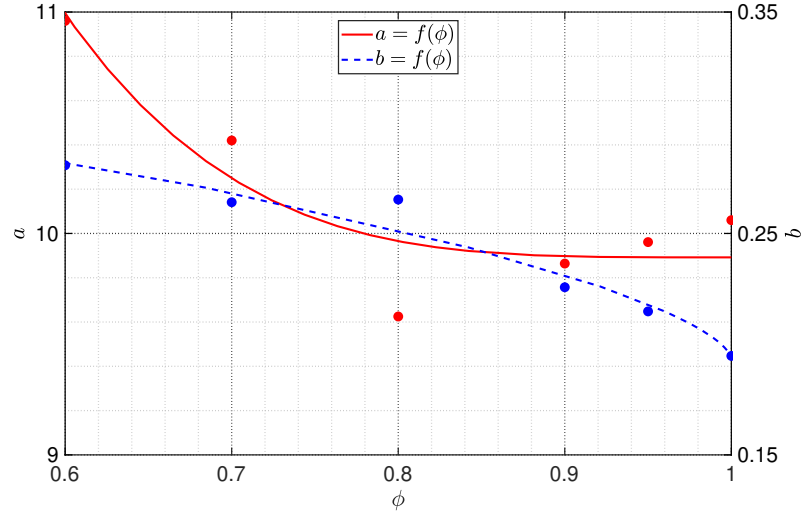


Figure 4.22: Effect of porosity on coefficients a and b ($Pr = 2$).

The coefficients a and b obtained for different porosities are plotted in Figure 4.22 to investigate the porosity dependency and obtain expressions for this coefficients. Expressions are reached and presented in 4.15 and 4.16.

$$a = 9.89 + 39.62(1 - \phi)^{3.91}, \quad (4.15)$$

$$b = 0.19 + 0.16(1 - \phi)^{0.62}, \quad (4.16)$$

In Figure 4.23 the data obtained in the numerical simulation for the multiple Prandtl numbers, and two different porosities ($\phi = 100\%$ and $\phi = 80\%$) are compared with the correlation obtained in this work 4.17. It can be seen that the expression agree well for a region of $Re_{p,L} > 30$ in the laminar steady regime. Can be concluded that the correlation achieved in the current work is better than those of Gamrat et al. [36] and Kuwahara et al. [28] to describe the Nusselt for a porous media with a Gyroid structure.

Final step is to combine the expressions and obtain the correlation with the Re , Pr and ϕ as variables. A universal correlation for the Nusselt number, which agrees well with available experimental data, has been established using the results obtained for a range of porosity, Prandtl and Reynolds numbers. The correlation obtained for the Gyroid surface, in the laminar steady regime, for a region $30 < Re_{p,L} < 150$, porosities $0.6 < \phi < 1.0$, and $0.7 < Pr < 7$ is the following:

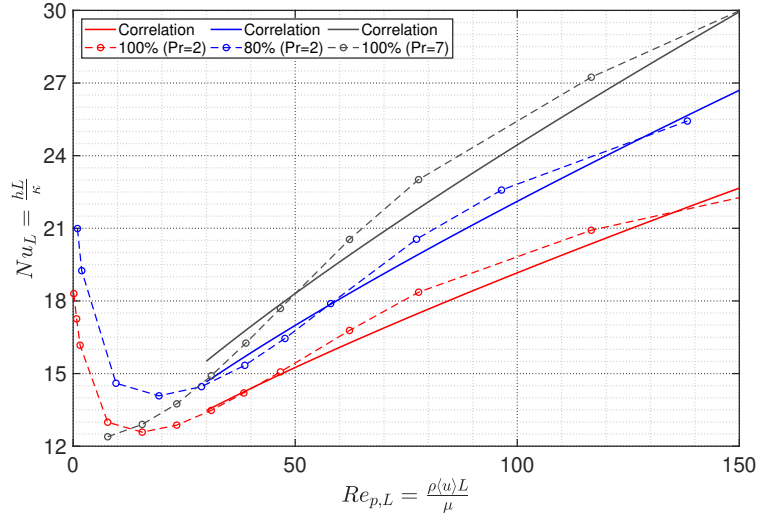


Figure 4.23: Correlation and results obtained comparison.

$$Nu_L = 9.89 + 39.62(1 - \phi)^{3.91} + (0.19 + 0.16(1 - \phi)^{0.62})Re_{p,L}^{0.79}Pr^{0.36}; \quad (4.17)$$

4.4 Heat exchanger thermal performance

In this Section, obtained results for the main parameters for the application of these geometries to heat exchangers are presented and analyzed. The approach followed is similar to the work presented by Passos [4]. The results presented were extended to the laminar-unsteady regime.

For the analysis of heat transfer in an internal flow, the principal parameter to be calculated is the Nu based on the hydraulic diameter as a function of $Re_{p,Dh}$ - Figure 4.24. One of the conditions of that analysis is that for the same surface and with a similar mass flow rate, but varying the porosity, both the hydraulic diameter and the interstitial velocity change, which leads us to conclude that the basis for comparison may not be the most appropriate [63]. To overcome this, in Figure 4.25, the Nu based on the length of the REV as a function of $Re_{Da,L}$ is shown. For the same mass flow rate and surface, Re is the same, regardless of the porosity of the geometry, which allows obtaining a better comparison.

In Figure 4.24, from $Re = 80 - 200$ the G60 geometry overcomes the counterpart G100 geometry in the value of the Nu_{Dh} . This behavior can be explained due to the transition from steady to unsteady flow starting earlier for the lower porosity, and the G100 geometry is still in the steady regime when the G60 is already in an unsteady flow regime. For the G and SD surface, when comparing the figures below, we can see that for higher porosities the Nu is higher with the definition of hydraulic diameter and lower with the characteristic length L , demonstrating that the performance comparison between surfaces and porosities depends on the definition used, and special care is needed as mentioned earlier. Figure 4.26 shows the variation of the heat transfer coefficient.

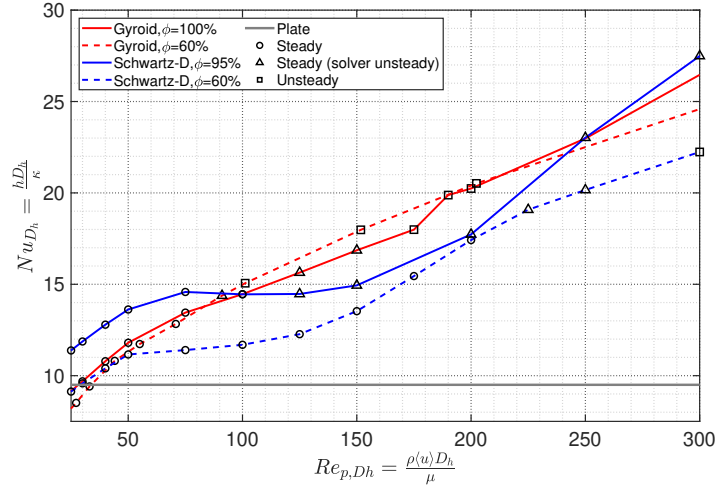


Figure 4.24: Nu_{Dh} vs $Re_{p,Dh}$.

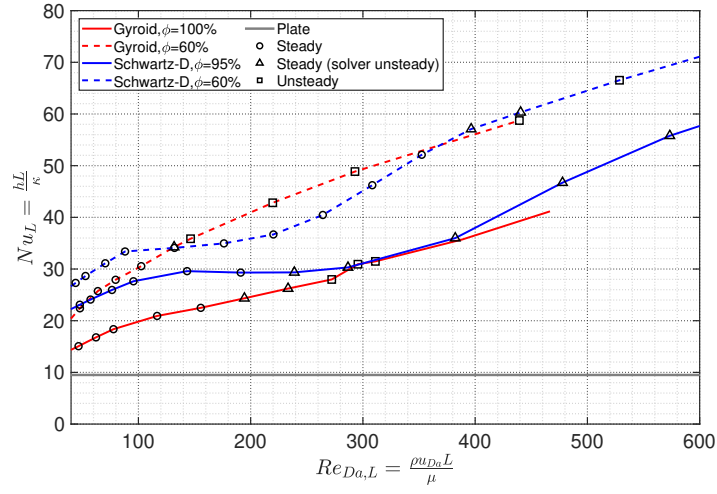


Figure 4.25: Nu_L vs $Re_{Da,L}$.

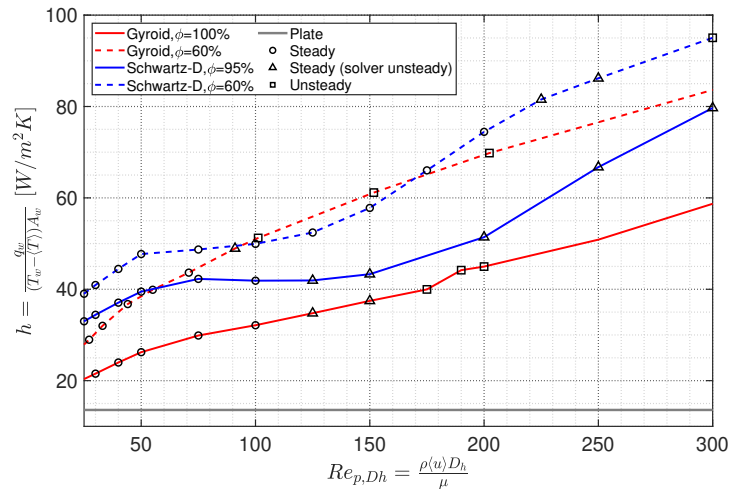


Figure 4.26: h vs $Re_{p,Dh}$.

Another way to make comparisons and that better reflects the convection in each geometry is Figure 4.27. Presents the energy density exchanged across the REV, i.e., heat transfer across the wall per volume.

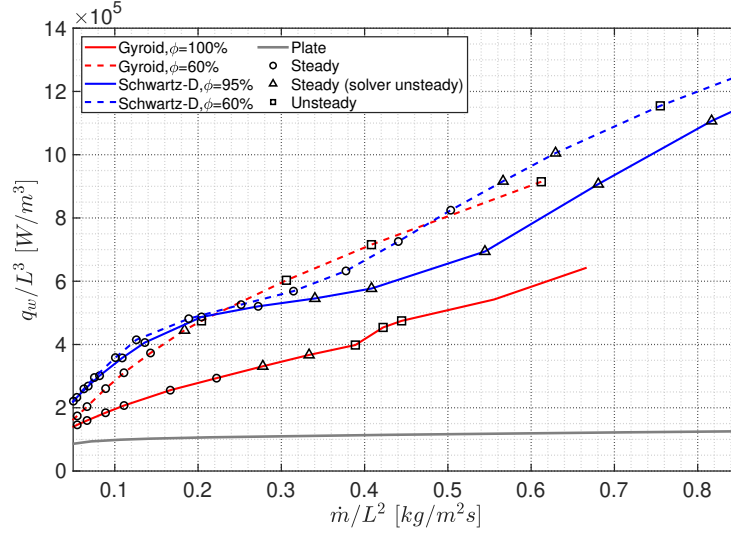


Figure 4.27: q_w/L^3 vs \dot{m}/L^2 .

Analyzing Figure 4.27 and comparing different surfaces with the same porosity, the G60 with the SD60 geometry. For the steady regime, the SD surface has a higher energy transfer than the G surface. The transition for the unsteady regime happens for a lower mass flow rate in the G60 geometry and for that reason, the energy exchanged overtakes the SD60 geometry. For a higher mass flow rate, both geometries are in the unsteady regime and the energy exchanged is highest again for the SD60 geometry. The TPMSs have superior convection properties to the full extent of the laminar steady regime, validating the results obtained by Passos [4]. After the transition to the unsteady laminar regime, the increase in convection properties of the TPMSs is even larger when compared with the flat plate that holds the laminar regime up to a $Re \approx 2000$ where the convection coefficient is constant. This means that the difference will be even larger in the turbulent flow regime.

To evaluate the efficiency of the heat transfer across the wall, the effectiveness parameter was calculated and presented in the next Figure 4.28. All of the TPMSs analysed have superior effectiveness in the unsteady regime compared to the parallel flat plate. The effectiveness is higher when the porosity is lower and tends to a constant value when reaching the unsteady flow.

The number of transfer units (NTU) is represented in the Figure 4.29 and is a combination of heat transfer coefficient, transfer area, fluid flow rate and heat capacity. It summarizes these dimensional parameters into one dimensionless parameter. The performance becomes a monotone function of this dimensionless parameter. Geometric and design parameters can be estimated with these dimensionless correlation.

With known NTU values, effectiveness can be found with a $\epsilon - NTU$ expression. In the previous Figures results obtained for the heat exchanger parameters were shown. The availability of $\epsilon - NTU$ data is very useful for predicting heat exchanger performance for more complex configurations with

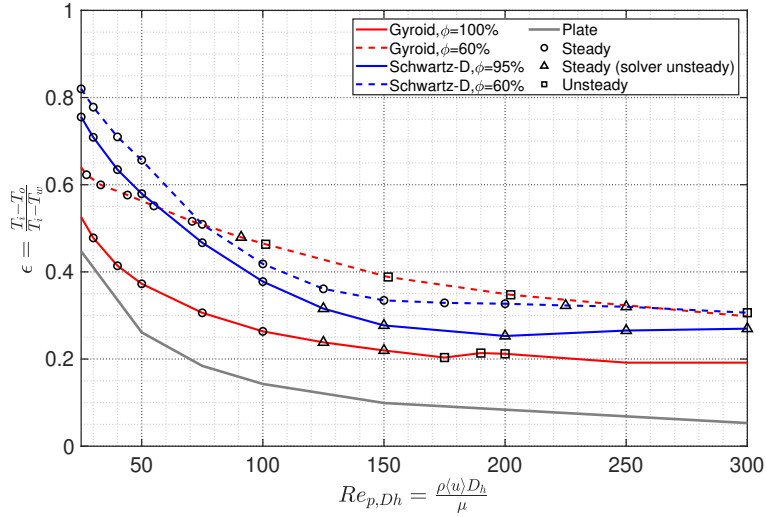


Figure 4.28: ϵ vs $Re_{p,Dh}$.

many different flow arrangements. This kind of heat exchanger can be approximate by the analytical expression 2.42. In the next Figure an analysis of the elaboration of the $\epsilon - NTU$ graphs obtained with the present simulations are presented.

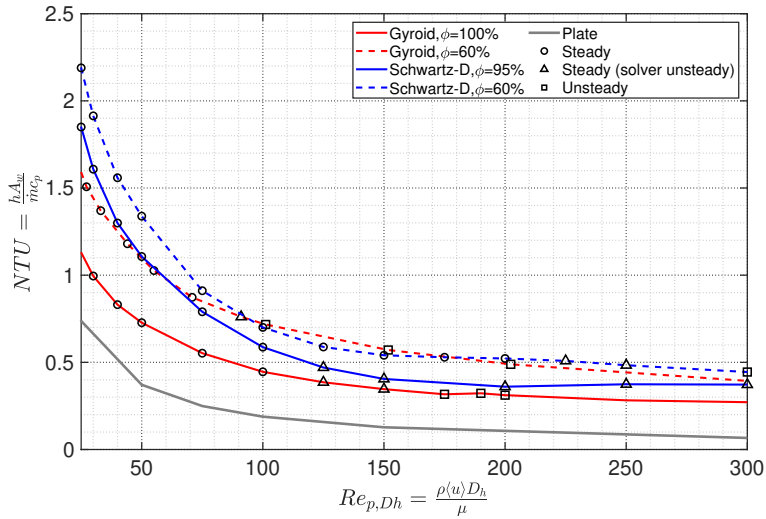


Figure 4.29: NTU vs $Re_{p,Dh}$.

For Figure 4.30 the solid gray curve correspond to the heat exchanger effectiveness analytical expression for a flow with constant wall temperature as explained in Section 2.3. We can see that the results obtained for the TPMS surfaces have a equal behavior of the analytical expression, that was the expected result. One important fact is illustrated: the use of a specific theoretical relation can introduce errors into different heat exchangers configurations.

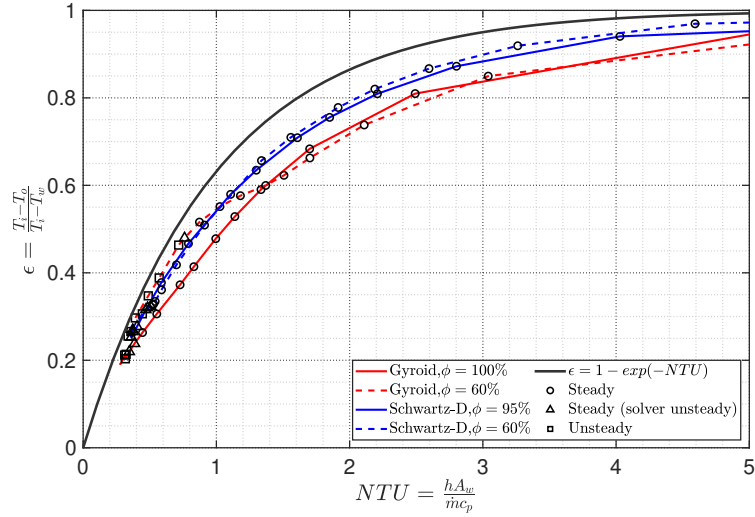


Figure 4.30: ϵ vs NTU .

In Figure 4.31 an optimization study for the maximization of the effectiveness and heat transfer per volume is presented. For a proper study, the inverse of energy density exchanged is shown in the x-axis (lower x value for a higher compatibility per heat transfer) and $1 - \epsilon$ plotted in the y-axis (lower y value for higher effectiveness). Analyzing the Figure, we can conclude that the points in the transition zone (solver unsteady) are a good choice because the line slope is accentuated. This means that a small increase in the energy density, the increase in the effectiveness is higher than in other zones for the same increase in the energy density.

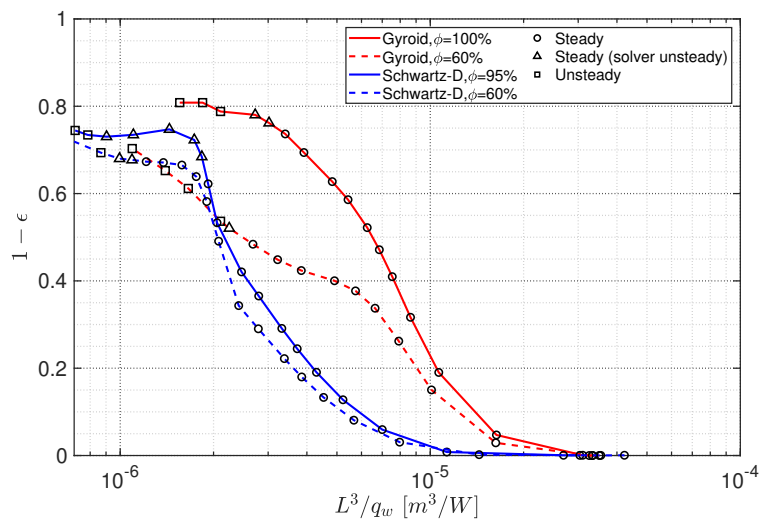


Figure 4.31: $1 - \epsilon$ vs L^3 / q_w .

4.4.1 Pareto Efficiency

The final study is to compare the energy trade-off between the heat exchanged (what one gets) and the pump power required to move the fluid across (what one pays).

In Figure 4.32 the ratio between the heat exchanged and the pump power (pressure drop) is shown. The parallel flat plate has the best performance than the TPMS for the steady and unsteady regime. This can be explained due to a minimal tortuosity in the flat plate that greatly influences the pressure drop. Comparing the Gyroid with the Schwartz-D surface, the former has a better ratio (trade-off) for the same porosity. The decrease in the wall thickness (higher porosity) has a higher wall surface while decreasing the pressure drop, resulting in a higher ratio for lower porosities. These results are in agreement with Passos [4].

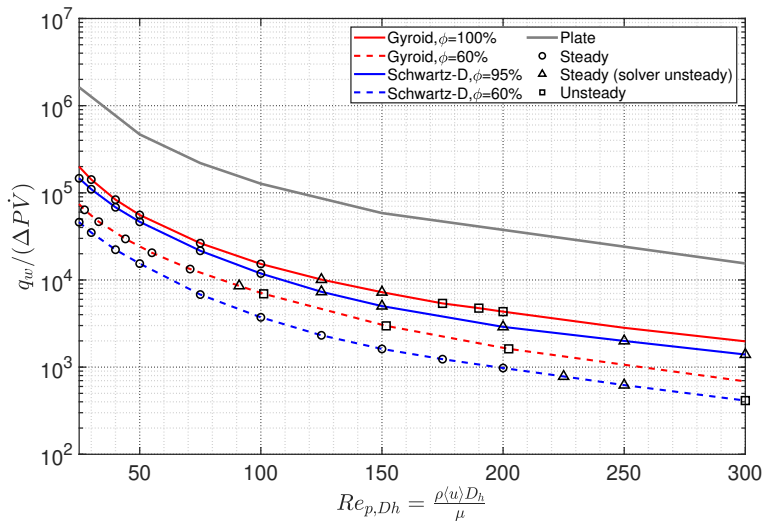


Figure 4.32: $q_w / (\Delta P \dot{V})$ vs $Re_{p,Dh}$.

A multi-objective optimization study (Pareto efficiency) is carried out to minimize the volume per heat transferred across the wall while minimizing pumping power.

Analyzing Figure 4.33, the parallel flat-plate has a better ratio between volume and heat exchanged at lower pumping power. With increasing pumping power the TPMS surpasses the flat plate performance and is the best solution when a high transfer rate is needed. The SD surface is the best choice for the steady regime allowing for greater heat transfer with lower space, and this conclusion is in agreement with the work of Passos and Femmer et al. [4, 15]. The unsteady regime is the main scope of this work and we can see that the conclusion is distinct from the steady regime because the G surface takes up the SD surface, holding both a very comparable ratio in this regime. For the equivalent pumping power and space used, a higher porosity has a higher energy transfer, besides the region when the G60 geometry has already transited for the unsteady regime and the G100 geometry is still in the steady regime. For this region, a lower porosity can have a better ratio.

Another interesting analysis to do is the comparison between multiple heat exchanger working fluids, i.e. between various Prandtl numbers. In Figure 4.34, the results achieved for the G100 geometry with $Pr = 7.0$ (water), and $Pr = 0.7$ (air) are displayed. An important conclusion is that for the water, one

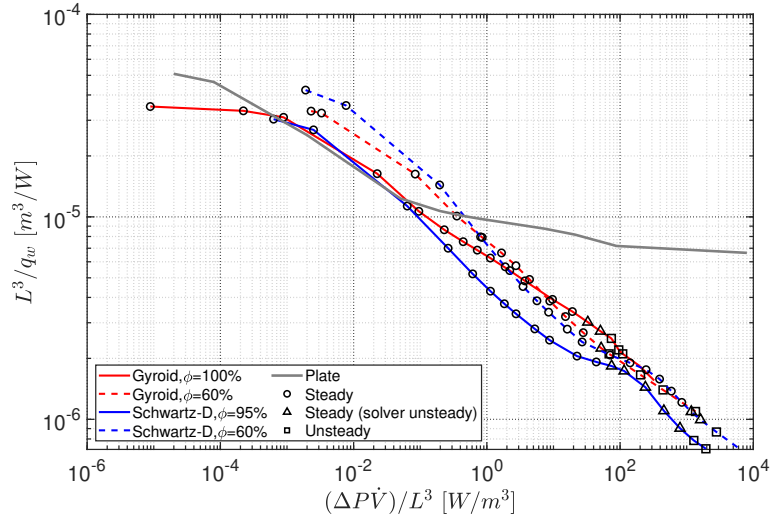


Figure 4.33: L^3/q_w vs $(\Delta P\dot{V})/L^3$ ($Pr = 2$).

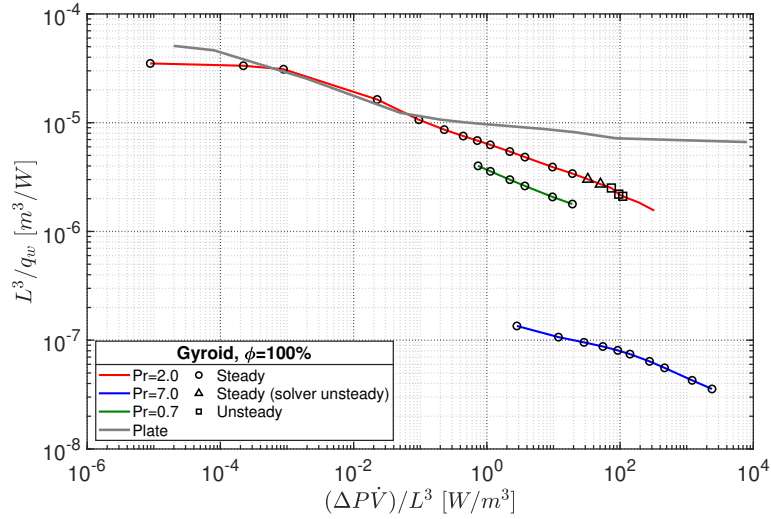


Figure 4.34: L^3/q_w vs $(\Delta P\dot{V})/L^3$ (Gyroid, $\phi = 100\%$).

of the most used working fluids in the industry of heat exchangers, the energy exchanged for the same pumping power is even greater in contrast with the flat plate. These results confirm once more that the use of TPMS for novel heat exchangers geometries is very promising.

From the results presented here in this Section, the SD surface presents itself as the best geometry for a laminar steady flow. To manufacture a heat exchanger, for a laminar unsteady flow, the choice can be between the two TPMS.

Chapter 5

Conclusions

Modeling of Triply Periodic Minimal Surfaces (Schwartz-D and Schoen-Gyroid) within a representative elementary volume with periodic boundaries was numerically investigated. Internal flow of pore-scale is considered throughout all the work. Multiple unit cubic cells were modeled on different positions, giving different structures for the representative elementary volume, in order to access the influence of the axial conduction in low velocity flows. For the same surface, different geometries are modeled for having different values of porosity and concluded about the influence of the geometric parameters on fluid flow.

The process of geometry creation was performed and subsequently imported to implement the numerical simulation and subsequent grid dependence and validation studies. The finite volume method code is adequate to solve pore-scale flow details using polyhedral cells, and the software Star-CCM+ is used. The concept of volume averaging ensured meaningful computational values and the computed parameters needed to study the pressure drop and heat transfer.

Transition to the laminar unsteady regime has studied and validated with the Forchheimer ratio between the inertial and total forces acting on the fluid inside the porous media. At lower porosities, the transition occurs at a lower mass flow rate inlet.

For the Nusselt number based on the characteristic length, a correlation is developed based on the porosity and Prandtl number as a function of the Reynolds. The present correlation bettered several weaknesses of the existing correlations for porous media, being more accurate for the Schoen-Gyroid surface.

An analysis of heat transfer in the laminar unsteady regime was made for the two different TPMS geometries and porosities. The heat transfer across the wall, thermal effectiveness, and pumping power was obtained and compared with the typical case of the parallel flat plate heat exchanger.

5.1 Achievements

The full process of geometry creation to numerical simulation was performed, and subsequent grid dependence and validation studies were completed to ensure proper discretization and model assumptions. An extensive study of the representative elementary volume position influence is performed. A

method with much less computational time to obtain the heat transfer parameters for low Péclet number is proposed. Transition points to laminar unsteady regime has obtained for the Schoen-Gyroid and related with the tortuosity and different Reynolds definitions. A correlation is developed and compared to literature correlations for the Schoen-Gyroid, with good results for the Nusselt number. Finally, another extensive study of the performance in the laminar Reynolds range is performed for different porosities.

5.2 Future Work

A few concepts for future work related to the topic presented in this thesis are presented:

- Extension of the data obtained in this work to the turbulent regime.
- Validation of the computational results with experimental data.
- Correlation extension to the laminar unsteady and turbulent regime using parameters like Strouhal number and kinetic turbulent energy.
- Compare the thermal performance of the surfaces analysed in this work with representative elementary volumes filled with random metal foams.
- Analyze the flow transition and heat transfer performance in others TPMSs.

Bibliography

- [1] BP statistical review of world energy. BP, 2019. 68th edition.
- [2] B. Zohuri. *Compact Heat Exchangers*, chapter 2. Springer International Publishing, Switzerland, 2017. ISBN 978-3-319-29835-1.
- [3] T. D. Ngoa, A. Kashania, G. Imbalzanoa, K. T. Nguyena, and D. Huib. Additive manufacturing (3D printing): A review of materials, methods, applications and challenges. *Composites Part B*, 143: 172–196, 2018. ISSN 1359-8368.
- [4] A. Passos. Laminar flow and heat transfer in triply periodic minimal surfaces. Master's thesis, Universidade de Lisboa, 2019.
- [5] Y. Jung and S. Torquato. Fluid permeabilities of triply periodic minimal surfaces. *Physical Review E*, 72, 2005. ISSN 1539-3755.
- [6] S. Maa, Q. Tanga, Q. Fenga, J. Songa, X. Hanb, and F. Guoa. Mechanical behaviours and mass transport properties of bone-mimicking scaffolds consisted of gyroid structures manufactured using selective laser melting. *Journal of the Mechanical Behavior of Biomedical Materials*, 93:158–169, 2019. ISSN 1751-6161.
- [7] H. Koh and C. L. Magee. A functional approach for studying technological progress: Application to information technology. *Technological Forecasting and Social Change*, 73:1061–1083, 2006. ISSN 0040-1625.
- [8] H. Darcy. Les fontaines publiques de la ville de dijon. Victor Dalmont, 1856. Taken from [4].
- [9] P. Forchheimer. P. wasserbewegung durch boden. Zeitschrift des Vereines Deutscher Ingenieur, 1901. Taken from [4].
- [10] S. Ergun. Fluid flow through packed columns. *Chemical Engineering Progress*, 48:89–94, 1952. ISSN 1945-0710.
- [11] A. Dybbs and R. V. Edwards. *A New Look at Porous Media Fluid Mechanics — Darcy to Turbulent*. Springer Netherlands, Dordrecht, 1984. ISBN 978-94-009-6175-3.
- [12] S. Whitaker. *Theory and Applications of Transport in Porous Media: The method of volume averaging, volume 13*. Springer Science & Business Media, 1999. ISBN 978-90-481-5142-4.

- [13] F. P. Incropera, D. P. DeWitt, T. L. Bergman, and A. S. Lavine. *Fundamentals of Heat and Mass Transfer 6th Edition*. Wiley, 2007. ISBN 978-0-471-45728-2.
- [14] S. Choi and J. Eastman. Enhancing thermal conductivity of fluids with nanoparticles. ASME International Mechanical Engineering Congress & Exposition, 1995.
- [15] T. Femmer, A. Kuehne, and M. Wessling. Estimation of the structure dependent performance of 3-D rapid prototyped membranes. *Chemical Engineering Journal*, 273:438–445, 2015. ISSN 1873-3212.
- [16] J. Pérez. A new golden age of minimal surfaces. *Notices of the American Mathematical Society*, 64:347–358, 2017. ISSN 0002-9920.
- [17] K. Michielsen and D. G. Stavenga. Gyroid cuticular structures in butterfly wing scales: Biological photonic crystals. *Journal of the Royal Society Interface*, 5:85–94, 2008. ISSN 1742-5662.
- [18] L. Han and S. Che. An overview of materials with triply periodic minimal surfaces and related geometry: From biological structures to self-assembled systems. *Advanced Materials*, 30:1–22, 2018. ISSN 1521-4095.
- [19] A. H. Schoen. Infinite periodic minimal surfaces without self-intersections. *Technical report, NASA Technical Notes*, 1970.
- [20] M. Kaviany. *Principles of heat transfer in porous media*. Springer-Verlag New York Inc, 1991. ISBN 978-1-4684-0412-8.
- [21] A. Calado. Laminar flow characterization in ceramic porous foams. Master's thesis, Universidade de Lisboa, 2016.
- [22] Available online April 2016. URL <http://specialpapers.gsapubs.org/content/404/177/F1.large.jpg>.
- [23] J. Bear and Y. Bachmat. *Introduction to Modeling of Transport Phenomena in Porous Media*. Springer-Verlag New York Inc, 1991. ISBN 978-94-009-1926-6.
- [24] S. Whitaker. Diffusion and dispersion in porous media. *AIChE*, 13:420–427, 1967. ISSN 1547-5905.
- [25] H. K. Versteeg and W. Malalasekera. *An Introduction to Computational Fluid Dynamics*. Pearson Education Limited, 2007. ISBN 978-0-13-127498-3.
- [26] L. Wang, L. P. Wang, Z. Guo, and J. Mi. Volume-averaged macroscopic equation for fluid flow in moving porous media. *International Journal of Heat and Mass Transfer*, 82:357–368, 2015. ISSN 1879-2189.
- [27] D. Ruth and H. Ma. On the derivation of the Forchheimer equation by means of the averaging theorem. *Transport in Porous Media*, 7:255–264, 1992. ISSN 0169-3913.

- [28] F. Kuwahara, M. Shirota, and A. Nakayama. A numerical study of interfacial convective heat transfer coefficient in two-energy equation model of porous media. *International Journal of Heat and Mass Transfer*, 44:1153–1159, 2001. ISSN 0387-5016.
- [29] M. Scheffler and P. Colombo. *Cellular ceramics: structure, manufacturing, properties and applications*. Wiley-VCH Verlag GmbH & Co. KGaA, Germany, 2006. ISBN 978-3-527-31320-4.
- [30] S. Whitaker. Flow in porous media i: A theoretical derivation of Darcy's law. *Transport in Porous Media*, 1:3–25, 1986. ISSN 1573-1634.
- [31] A. Hazen. Some physical properties of sand and gravels with special reference to their use in filtration. *Massachusetts State Board of Health*, 22:541, 1893. ISSN 0742-9010.
- [32] S. Ergun and A. Orning. A fluid flow through randomly packed columns and fluidized beds. *Industrial & Engineering Chemistry*, 41:1179–1184, 1949. ISSN 1943-2968.
- [33] D. D. Joseph, D. A. Nield, and Papanicolaou. Nonlinear equations governing flow in a saturated porous medium. *Water Resources Research*, 18:1049–1052, 1982.
- [34] S. Beavers and E. Sparrow. Influence of bed size on the flow characteristics and porosity of randomly packed beds of spheres. *Journal of Applied Mechanics*, 3:655–660, 1973. ISSN 1528-9036.
- [35] D. Seguin, A. Montillet, and J. Comiti. Experimental characterisation of flow regimes in various porous media, i: Limit of laminar flow regime. *Chemical Engineering Science*, 53(21):3751–3761, 1998. ISSN 1873-4405.
- [36] G. Gamrat, M. Favre-Marinet, and S. L. Person. Numerical study of heat transfer over banks of rods in small reynolds number cross-flow. *International Journal of Heat and Mass Transfer*, 51:853–864, 2008. ISSN 1879-2189.
- [37] W. M. Rohsenow, J. R. Hartnett, and Y. I. Cho. *Handbook of Heat Transfer*, 3rd ed. McGrawHill, 1998. ISBN 978-0-07-053555-8.
- [38] G. O. Brown. The history of the Darcy-Weisbach equation for pipe flow resistance. In *Environmental and Water Resources History*, 2012. ASCE Civil Engineering Conference and Exposition.
- [39] R. K. Shah and A. L. London. *Laminar Flow Forced Convection in Ducts: A Source Book for Compact Heat Exchanger Analytical Data*. Academic Press, 1978. ISBN 978-0-12-020051-1.
- [40] W. M. Kays and M. E. Crawford. *Convective Heat and Mass Transfer*, 3rd ed. McGraw-Hill, New York, 1993. ISBN 978-0-07-033721-7.
- [41] R. K. Shah and M. S. Bhatti. *Handbook of Single-Phase Convective Heat Transfer*, chapter 3. Wiley-Interscience, New York, 1987. ISBN 978-0-471-81702-3.
- [42] W. M. Kays and A. L. London. *Compact Heat Exchangers*, 3rd ed. McGraw-Hill, New York, 1984. ISBN 978-1-5231-2179-3.

- [43] K. Boomsma, D. Poulikakos, and Y. Ventikos. Simulations of flow through open cell metal foams using an idealized periodic cell structure. *International Journal of Heat and Fluid Flow*, 24:825–834, 2003. ISSN 1879-2278.
- [44] Z. Wang, H. Shang, and J. Zhang. Lattice boltzmann simulations of heat transfer in fully developed periodic incompressible flows. *Physical Review*, 95, 217. ISSN 1536-6065.
- [45] S. Krishnan, J. Y. Murthy, and S. V. Garimella. Direct simulation of transport in open-cell metal foam. *Journal of Heat Transfer*, 128, 2006. ISSN 1528-8943.
- [46] A. Diani, K. K. Bodla, L. Rossetto, and S. V. Garimella. Numerical investigation of pressure drop and heat transfer through reconstructed metal foams and comparison against experiments. *International Journal of Heat and Mass Transfer*, 88:508–515, 2015. ISSN 1879-2189.
- [47] A. D. Torre, G. Montenegro, G. R. Tabor, and M.-L. Wears. Cfd characterization of flow regimes inside open cell foam substrates. *International Journal of Heat and Fluid Flow*, 50:72–82, 2014. ISSN 1879-2278.
- [48] P. Parthasarathy, P. Habisreuther, and Zarzalis. A study of pressure drop in reticulated ceramic sponges using direct pore level simulation. *Chemical Engineering Science*, 147, 2016. ISSN 1873-4405.
- [49] J.-W. Luo, L. Chen, T. Min, F. Shan, Q. Kang, and W. Tao. Macroscopic transport properties of gyroid structures based on pore-scale studies: Permeability, diffusivity and thermal conductivity. *International Journal of Heat and Mass Transfer*, 146:118837, 2020. ISSN 1879-2189.
- [50] D. J. Yoo. Porous scaffold design using the distance field and triply periodic minimal surface models. *Biomaterials*, 32:7741–7754, 2011. ISSN 1878-5905.
- [51] Solidworks 3d cad, V.2018. Dassault Systemes.
- [52] Star-ccm+ user guide, V.2019. Siemens PLM Software.
- [53] M. Peric. Flow simulation using control volumes of arbitrary polyhedral shape. ERCOFTAC Bulletin, No. 62, 2004.
- [54] Ahmad, AboSerie, and Gaylard. Mesh optimization for ground vehicle aerodynamics. *CFD Letters*, 2:54–65, 2005. ISSN 2180-1363.
- [55] A. G. Dixon, E. Taskina, M. Nijemeisland, and H. Stitt. Wall-to-particle heat transfer in steam reformer tubes: Cfd comparison of catalyst particles. *Chemical Engineering Science*, 63:2219–2224, 2008. ISSN 0009-2509.
- [56] S. V. Patankar. *Numerical heat transfer and fluid flow*. CRC Press, 1980. ISBN 978-0-07-048740-5.
- [57] *Guide for the Verification and Validation of Computational Fluid Dynamics Simulations*, AIAA G-077. American Institute of Aeronautics and Astronautics, 1998. ISBN 978-1-56347-285-5.

- [58] P. Roache. *Verification and Validation in Computational Science and Engineering*. Hermosa Pub, 1998. ISBN 978-0-91-347808-3.
- [59] L. Wang, B. Sundén, and R. M. Manglik. *Plate Heat Exchangers*, chapter 1, pages 1–6. WIT Press, 2007. ISBN 978-1-85312-737-3.
- [60] F. E. Teruel and L. Díaz. Calculation of the interfacial heat transfer coefficient in porous media employing numerical simulations. *International Journal of Heat and Mass Transfer*, 60(9–10):307–327, 2013. ISSN 1879-2189.
- [61] A. Duda, Z. Koza, and M. Matyka. Hydraulic tortuosity in arbitrary porous media flow. *Physical Review E - Statistical, Nonlinear, and Soft Matter Physics*, 84, 2011. ISSN 1550-2376.
- [62] E. Werzner, C. D. Martin Abendroth, C. Settgast, D. Trimis, H. Krause, and S. Ray. Influence of foam morphology on effective properties related to metal melt filtration. *Advanced Engineering Materials*, 2017. ISSN 1527-2648.
- [63] C. Fee. 3D-printed porous bed structures. *Current Opinion in Chemical Engineering*, 18:10–15, 2017. ISSN 2211-3398.

